The Astrophysical Journal, 968:8 (23pp), 2024 June 10 https://doi.org/10.3847/1538-4357/ad410b

The Cosmic Ultraviolet Baryon Survey (CUBS). VII. On the Warm-hot Circumgalactic Medium Probed by O VI and Ne VIII at $0.4 \lesssim z \lesssim 0.7$

Zhijie Qu[1], Hsiao-Wen Chen[1], Sean D. Johnson[2], Gwen C. Rudie[3], Fakhri S. Zahedy[3], David DePalma[4,5], Joop Schaye[6], Erin T. Boettcher[7,8,9], Sebastiano Cantalupo[10], Mandy C. Chen[1], Claude-André Faucher-Giguère[11], Jennifer I-Hsiu Li[2,12], John S. Mulchaey[3], Patrick Petitjean[13], and Marc Rafelski[14,15]
[1] Department of Astronomy & Astrophysics, The University of Chicago, 5640 S. Ellis Avenue, Chicago, IL 60637, USA; quzhijie@uchicago.edu
[2] Department of Astronomy, University of Michigan, Ann Arbor, MI 48109, USA
[3] The Observatories of the Carnegie Institution for Science, 813 Santa Barbara Street, Pasadena, CA 91101, USA
[4] Department of Physics, MIT, 77 Massachusetts Avenue, Cambridge, MA 02139, USA
[5] MIT-Kavli Institute for Astrophysics and Space Research, 77 Massachusetts Avenue, Cambridge, MA 02139, USA
[6] Leiden Observatory, Leiden University, PO Box 9513, NL-2300 RA Leiden, The Netherlands
[7] Department of Astronomy, University of Maryland, College Park, MD 20742, USA
[8] X-ray Astrophysics Laboratory, NASA/GSFC, Greenbelt, MD 20771, USA
[9] Center for Research and Exploration in Space Science and Technology, NASA/GSFC, Greenbelt, MD 20771, USA
[10] Department of Physics, University of Milan Bicocca, Piazza della Scienza 3, I-20126 Milano, Italy
[11] Department of Physics & Astronomy, Center for Interdisciplinary Exploration and Research in Astrophysics (CIERA), Northwestern University, 1800 Sherman Avenue, Evanston, IL 60201, USA
[12] Michigan Institute for Data Science, University of Michigan, Ann Arbor, MI 48109, USA
[13] Institut d'Astrophysique de Paris, CNRS-SU, UMR 7095, 98bis bd Arago, Paris F-75014, France
[14] Space Telescope Science Institute, Baltimore, MD 21218, USA
[15] Department of Physics & Astronomy, Johns Hopkins University, Baltimore, MD 21218, USA
Received 2023 December 4; revised 2024 April 8; accepted 2024 April 12; published 2024 June 4

Abstract

This paper presents a newly established sample of 103 unique galaxies or galaxy groups at $0.4 \lesssim z \lesssim 0.7$ from the Cosmic Ultraviolet Baryon Survey (CUBS) for studying the warm-hot circumgalactic medium (CGM) probed by both O VI and Ne VIII absorption. The galaxies and associated neighbors are identified at <1 physical Mpc from the sightlines toward 15 CUBS QSOs at $z_{\rm QSO} \gtrsim 0.8$. A total of 30 galaxies or galaxy groups exhibit associated O VI $\lambda\lambda$ 1031, 1037 doublet absorption within a line-of-sight velocity interval of $\pm 250\,{\rm km\,s^{-1}}$, while the rest show no trace of O VI to a detection limit of $\log N_{\rm OVI}/{\rm cm^{-2}} \approx 13.7$. Meanwhile, only five galaxies or galaxy groups exhibit the Ne VIII $\lambda\lambda$ 770, 780 doublet absorption, down to a limiting column density of $\log N_{\rm NeVIII}/{\rm cm^{-2}} \approx 14.0$. These O VI- and Ne VIII-bearing halos reside in different galaxy environments with stellar masses ranging from $\log M_{\rm star}/M_\odot \approx 8$ to $\approx$11.5. The warm-hot CGM around galaxies of different stellar masses and star formation rates exhibits different spatial profiles and kinematics. In particular, star-forming galaxies with $\log M_{\rm star}/M_\odot \approx$ 9–11 show a significant concentration of metal-enriched warm-hot CGM within the virial radius, while massive quiescent galaxies exhibit flatter radial profiles of both column densities and covering fractions. In addition, the velocity dispersion of O VI absorption is broad with $\sigma_v > 40\,{\rm km\,s^{-1}}$ for galaxies of $\log M_{\rm star}/M_\odot > 9$ within the virial radius, suggesting a more dynamic warm-hot halo around these galaxies. Finally, the warm-hot CGM probed by O VI and Ne VIII is suggested to be the dominant phase in sub-L^* galaxies with $\log M_{\rm star}/M_\odot \approx$ 9–10 based on their high ionization fractions in the CGM.

Unified Astronomy Thesaurus concepts: Surveys (1671); Circumgalactic medium (1879); Quasar absorption line spectroscopy (1317); Galaxy evolution (594)

1. Introduction

The circumgalactic medium (CGM) is a multiphase gaseous reservoir surrounding galaxies. It spans a range in temperature and ionization conditions from the cool photoionized gas ($\log T/{\rm K} \approx 4$) to the collisionally ionized hot gas ($\log T/{\rm K} \approx 6$; see Donahue & Voit 2022; Faucher-Giguère & Oh 2023 for recent reviews). In this multiphase gas, the warm-hot phase at $\log T/{\rm K} \sim$ 5–6 is of particular importance in understanding the transformation of the CGM and its connection to galaxy evolution (e.g., Tepper-García et al. 2013; Oppenheimer et al. 2016; Rahmati et al. 2016; McQuinn & Werk 2018; Nelson et al. 2018; Stern et al. 2019; Faerman et al. 2020; Wijers et al. 2020, 2024; Ho et al. 2021; Appleby et al. 2023). The warm-hot gas may be short-lived in the CGM, compared to the cool and hot phases because of its high radiative emissivity (e.g., Oppenheimer & Schaye 2013; Gnat 2017). At the same time, it may be crucial for the survival or growth of cool clouds as an interface mixed in the hot gas (e.g., Gronke et al. 2022), making the warm-hot CGM potential fuel for future star formation in galaxies.

In observations, QSO spectroscopy is a powerful tool for characterizing the warm-hot gas by measuring highly ionized species (e.g., O VI and Ne VIII) in either local Universe (e.g., York 1974; Sembach et al. 2003; Lehner et al. 2011) at $z \approx 0.1$–1 (e.g., Savage et al. 2005; Danforth & Shull 2008; Thom & Chen 2008; Tripp et al. 2008; Mulchaey & Chen 2009; Narayanan et al. 2012; Meiring et al. 2013; Stocke et al. 2014; Johnson et al. 2015; Danforth et al. 2016; Qu & Bregman 2016; Werk et al. 2016; Burchett et al. 2019; Sankar et al. 2020;

Tchernyshyov et al. 2022) or $z \gtrsim 2$ (e.g., Bergeron et al. 2002; Simcoe et al. 2004; Muzahid et al. 2012; Rudie et al. 2019). In particular, O VI and Ne VIII are formed with respective ionization potentials of 113.9 and 207.3 eV, and destroyed at 138.2 and 239.1 eV. Under the assumption of collisional ionization equilibrium (CIE), O VI and Ne VIII exhibit ionization temperatures of $\log T/\mathrm{K} \approx 5.5$ and 5.8, respectively.

In principle, O VI and Ne VIII may also be photoionized by the ultraviolet background (UVB; e.g., Haardt & Madau 2001; Hussain et al. 2017; Khaire & Srianand 2019; Faucher-Giguère 2020) in the density range of $\log n_{\mathrm{H}}/\mathrm{cm}^{-3} \approx -6$ to -4. In practice, the low density of $\log n_{\mathrm{H}}/\mathrm{cm}^{-3} \lesssim -5$ is rarely seen in CGM in simulations (e.g., Rahmati et al. 2016). The expected low gas density implies a temperature of $\log T/\mathrm{K} > 4.5$ under photoionization equilibrium (PIE). Furthermore, a careful comparison of the line profiles of O VI and Ne VIII with low ions (e.g., O II and C II; tracing cool photoionized CGM of $\log T/\mathrm{K} \lesssim 4.5$) suggests that they are not in the same phase (e.g., Rudie et al. 2019; Zahedy et al. 2019; Cooper et al. 2021; Sameer & Norris 2021). Therefore, the O VI and Ne VIII absorption transitions trace the warm-hot gas at $\log T/\mathrm{K} > 4.5$ in the CGM, irrespective of the exact ionization mechanism.

In practice, O VI and Ne VIII are detected as strong doublet transitions at 1031, 1037 Å and 770, 780 Å, respectively, in the far-ultraviolet (FUV) band, which enable robust identifications of these highly ionized species based on the anticipated wavelength separation and doublet ratio. In addition, both oxygen and neon are α-elements with roughly constant relative abundance [Ne/O] and high abundances. Combining empirical constraints of these two ions, therefore, provides a sensitive probe of the physical conditions of the warm-hot CGM.

In the past few years, deep galaxy surveys have been performed in fields of distant UV bright QSOs with high-quality FUV spectra available for investigating the connection between galaxies and the CGM up to $z \approx 0.5$–1.0 (e.g., Fossati et al. 2019; Chen et al. 2020; Dutta et al. 2020; Lofthouse et al. 2020; Muzahid et al. 2021; Wilde et al. 2021), with the warm-hot gas being a significant component in these efforts (e.g., Chen & Mulchaey 2009; Johnson et al. 2015; Burchett et al. 2019; Tchernyshyov et al. 2022, 2023). As part of the Cosmic Ultraviolet Baryon Survey (CUBS) program (Chen et al. 2020), we are constructing a sample of galaxies from dwarfs with a stellar mass of $\log M_{\mathrm{star}}/M_{\odot} < 9$ to massive quiescent galaxies of $\log M_{\mathrm{star}}/M_{\odot} > 11$ in the redshift range of $z \approx 0.4$–0.7. All galaxies are selected based on their proximity to the QSO line of sight without any prior information on absorption features, leading to an unbiased sample for absorption property analysis. The redshift range of $z \approx 0.4$–0.7 is chosen to cover both the O VI and Ne VIII doublets in the high signal-to-noise ratio (S/N) FUV spectra obtained by the Hubble Space Telescope/Cosmic Origins Spectrograph (HST/COS; Green et al. 2012).

In this study, we investigate the properties of the warm-hot CGM traced by O VI and Ne VIII in galaxies spanning a broad range of environments. Section 2 summarizes the available data for both absorption spectroscopy and galaxy surveys, and presents the methodology used to extract galaxy and absorption properties. In Section 3, we investigate the association between absorption systems and galaxies, and the spatial distribution and kinematic properties of the warm-hot CGM. Further investigations of the dependence on galaxy properties are detailed in Section 4. In particular, we divide the entire galaxy sample into subsamples based on the stellar mass (M_{star}) and star formation rate (SFR), and report different trends of absorption properties for different galaxies (Sections 4.2 and 4.3). In Section 5, we compare the results with previous studies and discuss the implications for the origin of the warm-hot CGM. The key findings are summarized in Section 6. Throughout the paper, we adopt a Λ cosmology to calculate physical distances, assuming $\Omega_{\mathrm{m}} = 0.3$, $\Omega_{\Lambda} = 0.7$, and a Hubble constant of $H_0 = 70\,\mathrm{km\,s^{-1}\,Mpc^{-1}}$.

2. Data and Analysis

The CUBS program is designed to track the CGM evolution over a broad redshift range from $z \approx 0$ to ≈ 1 by combining high-quality QSO absorption spectra and deep galaxy survey data in the QSO fields (see Chen et al. 2020, for a complete description). Leveraging the CUBS data, we have established a new sample of 103 unique galaxies or galaxy groups at $0.4 \lesssim z \lesssim 0.7$, for which sensitive constraints can be obtained for both O VI and Ne VIII absorption properties in their CGM. The three-tier CUBS galaxy redshift survey provides ultradeep, deep-narrow, and shallow-wide coverage of the field around 15 near-UV bright QSOs at $z_{\mathrm{QSO}} > 0.8$ (see Chen et al. 2020 for definitions). This enables a detailed characterization of intervening galaxies and their surrounding environments along the QSO sightlines (e.g., Cooper et al. 2021). The CUBS intervening galaxy sample, spanning a wide range in mass from $\log M_{\mathrm{star}}/M_{\odot} \approx 8$ to ≈ 11.5 and a wide range in environments from isolated field galaxies to rich galaxy groups, provide a unique opportunity to study the O VI- and Ne VIII-bearing CGM in various galaxies.

2.1. QSO Absorption Spectra and Galaxy Survey Data

For each CUBS QSO, high-S/N HST/COS spectra were obtained using the medium-resolution (FWHM $\approx 20\,\mathrm{km\,s^{-1}}$) G130M and G160M gratings and multiple central wavelengths to yield contiguous spectral coverage from 1100–1800 Å (PID = 15163; PI: Chen). The spectra are processed and coadded using custom software, and the final combined spectra have a typical S/N of 12–31 per resolution element (see the details in Chen et al. 2018, 2020). The wavelength range of the final combined COS spectra provides simultaneous coverage of the O VI and Ne VIII doublets over the redshift range of $0.43 \lesssim z \lesssim 0.72$.

To establish a blind sample of intervening galaxies in this redshift range, we identify galaxies at projected distances $d \lesssim 1$ Mpc from the CUBS deep-narrow survey component that was carried out using a combination of the Multi Unit Spectroscopic Explorer (MUSE; Bacon et al. 2010), an integral field spectrograph on the Very Large Telescope and Low Dispersion Survey Spectrograph 3 (LDSS3C), a high-efficiency optical multi-object spectrograph and imager on the Magellan Telescopes (see Chen et al. 2020; Cooper et al. 2021). While the LDSS3C component reaches a limiting magnitude of $m_{r,\mathrm{AB}} \approx 24$ out to ≈ 1 Mpc at $z \approx 0.5$, the MUSE observations provide the deepest view in the inner 200 kpc around the QSO with a limiting pseudo-r magnitude of $m_{r,\mathrm{AB}} \approx 26.0$. These spectroscopic data enable secure galaxy redshift measurements based on clearly detected spectral features (see Qu et al. 2023 for details; hereafter CUBS VI). We also include additional spectroscopic redshift survey data from the shallow-wide component, which reaches a limiting magnitude of $m_{r,\mathrm{AB}} \approx 22.5$ out to ≈ 4 Mpc at

$z \approx 0.5$ using Inamori-Magellan Areal Camera & Spectrograph (IMACS) multislit observations. These are useful for characterizing the large-scale environment of those galaxies found closer to the QSO sightlines.

In addition to the spectroscopic survey data, deep optical have been obtained using LDSS3C and IMACS, a wide-field imager and spectrograph; Dressler et al. 2011), and near-infrared images using FourStar (a wide-field near-infrared imaging camera; (Persson et al. 2013) on the Magellan telescopes. These images reach 5σ limiting magnitudes of ≈26.0, 25.5, 25.5, 25.5, and 24.5 in the g, r, i, z, and H bands, respectively. They provide additional constraints on the broadband spectral energy distributions (SEDs) of individual galaxies. In particular, we estimate the stellar mass for all galaxies with secure redshifts and five-band optical and near-infrared photometry available (D. DePalma et al. 2024, in preparation), using Bayesian Analysis of Galaxies for Physical Inference and Parameter EStimation package (`BAGPIPES`; Carnall et al. 2018). We adopt the Kroupa (2001) initial mass function for this exercise (see CUBS VI for the details). This exercise leads to a sample of 1657 galaxies with $\log M_{\rm star}/M_{\odot} \approx 8$–11.5 at $z \approx 0.4$–0.7 in the CUBS galaxy survey.

The faintest galaxies in the CUBS galaxy sample are spectroscopically identified in the MUSE observations, the deepest spectroscopic survey component in the CUBS program. As a result, the majority of these faint galaxies are not detected in the Magellan imaging survey, and only pseudo-g-, r-, and i-photometric measurements are available from MUSE (e.g., Chen et al. 2020). Constraints for $M_{\rm star}$ of these galaxies, therefore, rely on a color–magnitude analysis described in the following two paragraphs.

To ensure that $M_{\rm star}$ is determined consistently for both bright and faint galaxies, we define a calibration galaxy sample that has both pseudo-g, r, i photometry from MUSE and g-, r-, i-, z-, and H-band photometric measurements from Magellan. While using g-, r-, and i-band photometry alone does not provide as strong a constraint on $M_{\rm star}$ as using a combination of optical and near-infrared photometry, the three optical bands together can still place robust constraints on the rest-frame B-band absolute magnitudes (M_B) and $u-g$ colors for galaxies at $z \approx 0.4$–0.7. The utility of this calibration sample is, therefore, to explore the possibility of constraining $M_{\rm star}$ using a combination of M_B and $u-g$ for all galaxies in our sample (e.g., Huang et al. 2016).

We first calculate the rest-frame M_B and $u-g$ by incorporating only available observed g-, r-, and i-band photometry for each galaxy using the `kcorrect` software (Blanton & Roweis 2007). Next, we derive an empirical relation that best characterizes the correlation between the `BAGPIPES`-inferred $M_{\rm star}$ and the rest-frame M_B and $u-g$ color. To account for the blue and red sequences in the galaxy population as a result of differences in star formation history (e.g., Chen et al. 2010; Johnson et al. 2015), we consider two different branches in the $M_{\rm star}$ and color–magnitude correlation. We find that for blue galaxies with $u-g < 0.9$

$$\log M_{\rm star}/M_{\odot} = -(0.36 \pm 0.02)M_B + (2.17 \pm 0.05)(u-g) + (1.1 \pm 0.3), \quad (1)$$

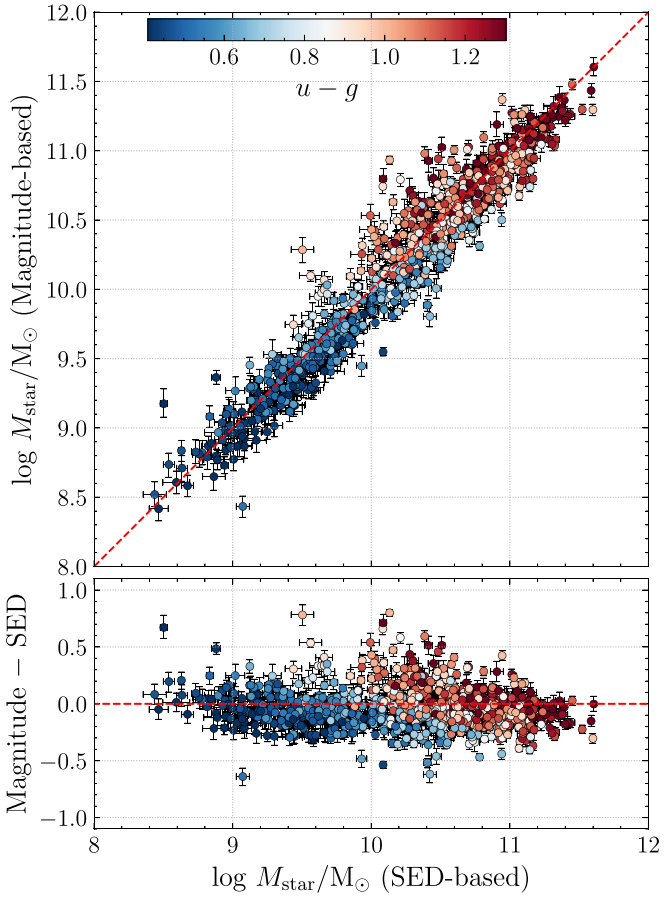

Figure 1. Comparison between the SED-based and magnitude-based stellar masses. The intrinsic scatter of the empirical relation between $M_{\rm star}$, M_B, and $u-g$ color is ≈0.2 dex, which is determined using 910 galaxies at $z \approx 0.4$–0.7 with high-quality observed magnitudes, leading to derived $M_{\rm star}$ uncertainties of <0.1 dex.

and for red galaxies with $u-g \geqslant 0.9$

$$\log M_{\rm star}/M_{\odot} = -(0.36 \pm 0.02)M_B + (0.72 \pm 0.05)(u-g) + (2.4 \pm 0.3). \quad (2)$$

The best-fit coefficients are determined using a Bayesian framework described in Qu et al. (2022). To determine the intrinsic scatter of this empirical relation, we select 910 galaxies at $z \approx 0.4$–0.7 with well-measured magnitudes by filtering out galaxies with $M_{\rm star}$ uncertainties larger than 0.1 dex. Using this high-quality galaxy sample, the residuals between the mean relation and the data exhibit a scatter of ≈0.2 dex over the covered stellar mass range of $\log M_{\rm star}/M_{\odot} \approx 8$–11.5 (Figure 1). The best-fit empirical relation is applied to all foreground galaxies for estimating $M_{\rm star}$ from the observed g, r, and i magnitudes.

In total, the CUBS galaxy sample consists of 11,593 spectroscopically identified foreground galaxies with available g, r, and i magnitudes at $z_{\rm gal} > 0.01$ and line-of-sight velocity of >5000 km s^{-1} away from the QSO emission redshift. These galaxies are projected within ≈5 Mpc around QSO sightlines. For these galaxies, the derived $M_{\rm star}$ spans the range of $\log M_{\rm star}/M_{\odot} \approx 8$–11.5. We also compute an inferred dark matter halo mass using a stellar mass–halo mass (SMHM) relation at $z \lesssim 1$. We adopt the relation from Behroozi et al. (2019)

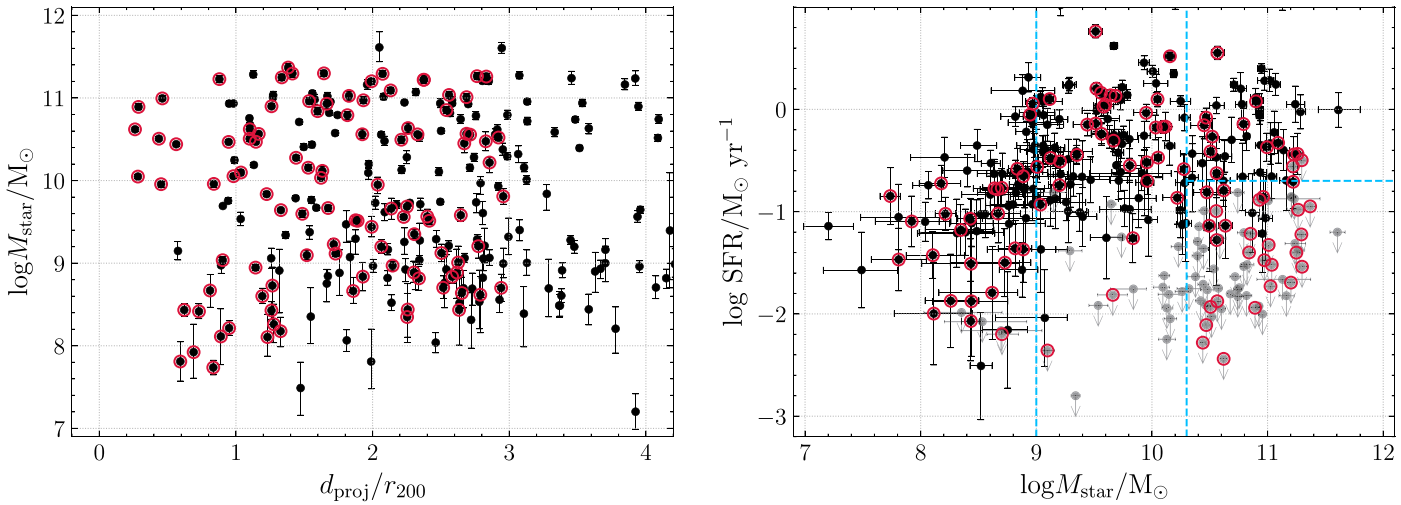

Figure 2. Summary of the general galaxy characteristics of the CUBS sample at $0.4 \lesssim z \lesssim 0.7$, including virial-normalized projected distance ($d_{\rm proj}/r_{200}$), stellar mass ($M_{\rm star}$), and SFR. Derived stellar masses have systematic uncertainties of 0.2 dex over the covered $M_{\rm star}$. For each galaxy group, the open red circle marks the galaxy with the smallest $d_{\rm proj}/r_{200}$ from the QSO sightline. In this sample, most galaxies are star-forming with specific SFRs (sSFRs) of $\geqslant 10^{-11}$ yr^{-1}. In addition, the entire sample is split into four subsamples in the following analysis, i.e., the dwarf, sub-L^*, massive star-forming, and massive quiescent galaxy samples (see Section 4.2), which are classified using the dashed blue boundaries in the right panel.

and account for the missing light described in Kravtsov et al. (2018) for all redshifts. The halo radius (r_{200}) is approximated using r_{200}, within which the mean dark matter density is 200 times the cosmic critical density.

In addition to the stellar and halo mass estimation, we also extract SFRs using the detected nebular lines in galaxy spectra. Specifically, we adopt the equivalent widths (EWs) of two nebular lines, the [O II] doublet, and Hβ, as tracers of SFR. For these two features, we adopt the spectral windows defined in Yan et al. (2006) to calculate the EWs. For Hβ, we infer EW(Hα) using the anticipated line ratio of EW(Hα)/EW(Hβ) ≈ 2.8. Then, the line luminosities of [O II] and Hα are calculated by combining EW and rest-frame magnitudes (u and g), and are converted into SFRs using the empirical conversion described in Kewley et al. (2004) and (Fumagalli et al. 2012, originated from Kennicutt 1998) for [O II] and Hα, respectively. The [O II]-based SFR is adopted for a galaxy when both [O II] and Hβ are available. Among all 11,593 galaxies in the CUBS program, 9130 and 2358 have SFRs determined based on [O II] and Hβ, respectively. For the remaining 105 galaxies, neither spectral feature is available, due to gaps in the optical spectra.

2.2. CUBS-midz: A New Galaxy Sample for Probing the Warm-hot CGM at $0.4 \lesssim z \lesssim 0.7$

Here, we introduce a new sample of intermediate-redshift galaxies assembled from the entire CUBS galaxy sample for investigating the warm-hot CGM at $0.4 \lesssim z \lesssim 0.7$ (hereafter designated as the CUBS-midz sample). The redshift range is dictated by a simultaneous spectral coverage of the O VI and Ne VIII doublets in the COS/FUV spectra. A two-step procedure is adopted to select galaxies based on their proximity to the QSO sightlines. First, we select all galaxies at projected distances ($d_{\rm proj}$) less than $3r_{200}$ from the QSO sightlines, leading to a sample of 212 individual galaxies. For these 212 galaxies, we then define overdense regions based on the number of galaxies with line-of-sight velocity separations of $|\Delta v| < 500$ km s^{-1} and projected separations of $d_{\rm proj} \lesssim 1$ Mpc from the QSO sightlines. We identify 60 isolated galaxies with no neighbors found in the immediate vicinity and 43 unique overdense regions with more than one galaxy identified in the search volume, leading to a total of 103 unique galaxies or galaxy groups in this new sample.

To further characterize the galaxy environment, we expand the search of associated galaxies beyond the initial $d_{\rm proj} < 3r_{200}$ from the QSO sightlines. Specifically, we search for all nearby galaxies with projected separations of $d_{\rm proj} \lesssim 3r_{200}$ and a velocity difference of $\lesssim 2\, v_{\rm vir}$ from the galaxies in the initial CUBS-midz sample. This second iteration led to the identification of additional neighbors, reducing the number of isolated galaxies to 50 and increasing the number of sightlines probing overdense environments to 53. Hereafter, we use galaxy groups referring to overdense environments with multiple nearby galaxies, although some systems are ambiguous to be identified as galaxy groups or not.

In summary, this exercise establishes the final sample of 304 galaxies that form 103 unique galaxies or galaxy groups (summarized in Table B1 in Appendix B). The number of galaxies in the galaxy groups ranges from 2–21, with half of the groups containing more than four members. Figure 2 summarizes the ranges of $d_{\rm proj}/r_{200}$ to the QSO sightlines, $M_{\rm star}$, and SFR of the full CUBS-midz sample. In particular, these galaxies span a range in $\log M_{\rm star}/M_\odot \approx$ 7–11.5 and SFR from $\lesssim 10^{-2}$ to $10\, M_\odot$ yr^{-1}. For each system, the galaxy with the smallest $d_{\rm proj}/r_{200}$ to the QSO sightlines is highlighted with an open red circle.

In this CUBS-midz sample, several galaxies and galaxy groups have been studied in previous CUBS papers, but none have published constraints on the properties of Ne VIII. Specifically, the new sample includes the galaxy group hosting an H_2-bearing damped Lyα absorber (DLA) at $z_{\rm DLA} = 0.57$ presented in CUBS II (Boettcher et al. 2021), three galaxies or galaxy groups hosting a Lyman limit system (LLS) at $z_{\rm LLS} = 0.4$–0.6 presented in CUBS III (Zahedy et al. 2021), and two galaxy groups each hosting a partial LLS (pLLS) at $z_{\rm pLLS} = 0.47$–0.54 reported in CUBS IV (Cooper et al. 2021).

2.3. Absorption Measurements

Having established a new CUBS-midz galaxy sample at $z \approx 0.4$–0.7, we proceed with searches for O VI and Ne VIII absorption features within a line-of-sight velocity of 1000 km s^{-1} for each galaxy or member galaxies in each galaxy group. The velocity window corresponds to roughly twice the escape velocity of the most massive galaxies in the sample. For our study, we search not only for O VI and Ne VIII absorption features, but also for low-ionization transitions, such as H I, O IV, and O V, to guide the identifications of O VI and Ne VIII based on matching kinematic absorption profiles. While these low ions may not share similar component ratios with O VI or Ne VIII, all detected O VI and Ne VIII features in the new sample have detectable H I or other low-ionization transitions. We require that the detected O VI or Ne VIII absorption features exhibit matched doublet line ratios without significant contamination and that both lines are detected at $\gtrsim 2\sigma$. If one of the doublet members is significantly contaminated, then we consider this absorption as an upper limit. If both members are contaminated, then no constraints are available for the absorption.

Next, we measure the absorption properties for O VI and Ne VIII doublets using the Voigt profile fitting method described in (Qu et al. 2022, see also Zahedy et al. 2016). The observed features of O VI and Ne VIII are decomposed into a minimum number of absorption components as required by the line profiles. Then, each component is modeled based on a Voigt function, characterized by the ion column density, Doppler b parameter, and line centroid. A canonical 2:1 ratio is adopted to fit both doublet members simultaneously. For nondetections, we obtain a 2σ upper limit for the column density with the line centroid fixed to either the systemic redshift of the galaxy or the redshift at the associated low-ionization transitions. For galaxy groups with nondetected absorption, the line centroid is fixed to the redshift of the galaxy with the smallest $d_{\rm proj}/r_{200}$. The b parameters of nondetections are fixed to 30 km s^{-1}, typical of known O VI and Ne VIII absorbers from previous studies (e.g., Werk et al. 2013; Savage et al. 2014; Johnson et al. 2015; Zahedy et al. 2019).

We compute the line-of-sight properties of the warm-hot CGM based on the integrated absorption properties of O VI and Ne VIII. Specifically, we extract the total column density (N) as the summation of all individual absorption components. Furthermore, we calculate the velocity centroid ($v_{\rm c}$) and the line-of-sight velocity dispersion (σ_v) for each ion following

$$v_{\rm c} = \frac{\sum N(v)v}{N},$$
$$\sigma_v^2 = \frac{\sum N(v)(v - v_{\rm c})^2}{N}, \quad (3)$$

where $N(v)$ is the column density of the modeled Voigt profile in each velocity bin, and the zero velocity is selected to be the redshift of the galaxy with the smallest $d_{\rm proj}/r_{200}$ (see the discussion in Section 3.1).

Note that the velocity dispersion calculated from the second moment has different physical implications in different absorption systems. When it is a single-component system, the calculated velocity dispersion is related to b of that component according to $\sigma_v = b/\sqrt{2}$. In this case, the measured velocity dispersion represents the combined thermal and nonthermal motions within an absorbing cloud. If multiple components are detected, the velocity dispersion is dominated by the projected velocity difference between different components, which measures the large-scale relative motion between clumps. In the following analysis, we designate absorption with $\sigma_v \geqslant 40$ km s^{-1} as broad features, which mainly trace the inter-cloud kinematics because the observed maximum b value is $\approx$60 km s^{-1} for individual O VI components (e.g., Werk et al. 2013; Savage et al. 2014; Zahedy et al. 2019).

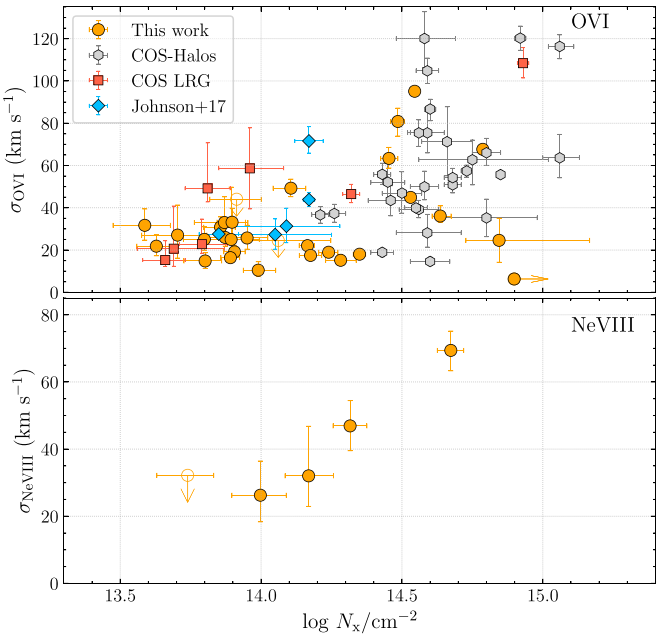

Figure 3. Summary of the line-of-sight total column density and the velocity dispersion for detected O VI (top panel) and Ne VIII features (bottom panel). In this plot, we also include the COS-Halos (gray hexagons; Werk et al. 2013), J17 (blue diamonds), and COS-LRG samples (red squares; Zahedy et al. 2019). All detected O VI features exhibit column densities of $\log N/{\rm cm}^{-2} \gtrsim 13.5$, while broad features ($\sigma_v \geqslant 40$ km s^{-1}) mostly have $\log N/{\rm cm}^{-2} \gtrsim 14.5$. For Ne VIII, broad features have higher column densities, but the significance of this trend is limited by the small sample.

3. The Warm-hot CGM Around Galaxies

The analysis described in Section 2 returns detections of O VI in 30 galaxies or galaxy groups, while only five display associated Ne VIII absorption features. For the remaining sample, we place a 2σ upper limit, assuming $b = 30$ km s^{-1}, to the underlying ionic column densities at the locations of individual galaxies/galaxy groups. Figure 3 shows that the detected absorbers have ionic column densities spanning from $\log N/{\rm cm}^{-2} = 13.5$–$15.0$ for both O VI and Ne VIII, and the corresponding velocity dispersions vary from $\sigma_v \approx$ 5–120 km s^{-1}.

Here, we also consider previously published galaxy samples for characterizing the O VI-bearing gas, including an IMACS survey from the Johnson et al. (2017, hereafter J17) sample, the COS-Halos survey (Werk et al. 2013), the COS-LRG survey (Zahedy et al. 2019), and the CGM^2 survey (Tchernyshyov et al. 2022) for O VI. The CASBaH sample is not included for comparisons in Figure 3 because neither the best-fit b values nor the velocity dispersions of Ne VIII were reported (Burchett et al. 2019). However, it will be included in comparisons of the column density profiles. We find that broad absorption features with $\sigma_v > 40$ km s^{-1} occur primarily in strong absorbers with

$\log N/\mathrm{cm}^{-2} > 14.5$, indicating complicated kinematics in these systems.

In this section, we first explore whether and how any galaxy properties are correlated with the observed strength of the O VI and Ne VIII absorbers. Specifically, we examine the significance of the correlation between absorption properties and a combination of different host galaxy assignments, including the galaxy at the smallest $d_{\rm proj}$, the galaxy at the smallest r_{200}-normalized $d_{\rm proj}$, and the most massive member in a galaxy group. Next, we examine the covering fraction and gas kinematics of the warm-hot CGM probed by O VI and Ne VIII.

3.1. Connecting Absorbers to Galaxies in the Presence of Neighbors

As summarized in Section 2.2, 53 unique galaxy groups containing between two and 21 members are identified in the CUBS-midz sample. This subsample of galaxy groups provides an exciting opportunity to study the warm-hot CGM in overdense galaxy environments based on observations of O VI and Ne VIII absorption. In an overdense environment, however, the association of absorption features with individual members of the group becomes more ambiguous. By comparing the mean properties of the galaxy groups, such as the center of mass, previous studies have shown that the O VI-bearing gas is more likely to be associated with individual galaxies rather than the intragroup medium (e.g., Stocke et al. 2014, 2017). However, other studies also suggest that the galactic environments could regulate the properties of absorbing gas (e.g., Johnson et al. 2015; Pointon et al. 2017; Dutta et al. 2021). We will discuss the general impact of the galactic environment in future studies. Here, we apply the new CUBS-midz sample, including isolated and nonisolated galaxies, to explore galaxy-absorber connections in the presence of neighbors.

In particular, we test the correlation between the light-of-sight absorption characterization and galaxy properties of different nearby galaxies. In Figure 4, we show, respectively, the spatial profiles of O VI absorption column densities for different host galaxy assignments. Because few galaxies/galaxy groups display detectable Ne VIII absorption, no clear trend can be established for any of the host galaxy assignments (see Figure A1 in Appendix A).

From the top to bottom panels, we consider the closest galaxy at the smallest $d_{\rm proj}$ in each galaxy group, the galaxy with the closest r_{200}-normalized projected distance (minimum $d_{\rm proj}/r_{200}$), and the most massive member of the group (maximum $M_{\rm star}$). Here, virial radii are calculated for individual galaxies in each galaxy group. As a comparison, we also show the isolated galaxy sample in the rightmost panels. In the left and right panels, the radial profiles are plotted as functions of $d_{\rm proj}$ and $d_{\rm proj}/r_{200}$, respectively. In each galaxy panel, we calculate the correlation coefficient τ using a generalized Kendall's rank order test, including both measurements and limits, and quantify the significance of the correlation between the absorbing column density and the projected distance. Using the Kendall rank order technique, a perfect correlation would result in a correlation coefficient of 1, whereas no correlation or an anticorrelation would be 0 or -1, respectively. The results are summarized in Table 1.

Among the three different galaxy assignments, linking the O VI absorption to the most massive member of the group exhibits the weakest correlation with either $d_{\rm proj}$ or $d_{\rm proj}/r_{200}$. A generalized Kendall's test returns a rank coefficient of

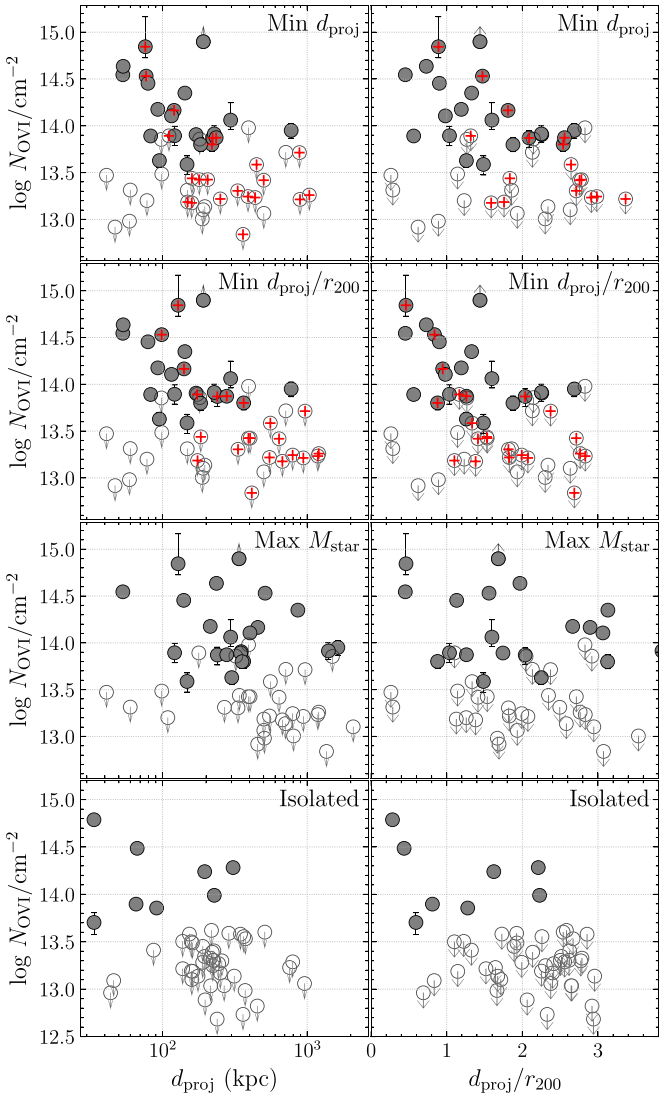

Figure 4. Spatial profiles of O VI column density constructed based on different assignments of associated galaxies and projected absorber-galaxy distances. $N_{\rm OVI}$ is most strongly correlated with galaxies with the smallest $d_{\rm proj}/r_{200}$, where r_{200} is calculated for individual galaxies (see Table 1 for the statistics). We present the dependence of column density on the projected distance and the r_{200}-normalized distance in the left and right panels, respectively. Error bars represent 68% confidence intervals of the column density measurements, and downward arrows represent the 95% upper limits for nondetections. In one case, the O VI absorber appears to be saturated, which is indicated by an upward arrow. In overdense galaxy environments, three different galaxy associations are explored, including the galaxy at the smallest $d_{\rm proj}$, the galaxy at the smallest $d_{\rm proj}/r_{200}$, and the galaxy with the highest $M_{\rm star}$ from top to bottom in the first three rows. The isolated galaxy sample is plotted in the lowest row for comparison. In the first two rows, the physically closest galaxy is also the one with the smallest $d_{\rm proj}/r_{200}$ in 31 galaxy groups. For the remaining 22 groups, we highlight the difference in the associated galaxies using red plus symbols. Overall, the combination of adopting the galaxies at the smallest $d_{\rm proj}/r_{200}$ and r_{200}-normalized distance yields the tightest correlation (right panel in the second row).

$|\tau| < 0.25$ ($<2\sigma$). This weak correlation is similar to what was found for the cool CGM in CUBS VI. Furthermore, we examine whether galaxies at the smallest $d_{\rm proj}$ or $d_{\rm proj}/r_{200}$ exhibit a tighter correlation with the observed absorption properties. In general, we find that adopting the galaxies at the smallest $d_{\rm proj}/r_{200}$ slightly improves the significance of the anticorrelation, in comparison to adopting the galaxies at the

Table 1
Summary of Statistics in Different Galaxy Associations

Ion	Galaxy	Physical[a]		r_{200}-Normalized[a]	
		τ[b]	Sig.[b]	τ[b]	Sig.[b]
O VI	Min $d_{\rm proj}$	−0.245	2.0σ	−0.277	2.3σ
O VI	Min $d_{\rm proj}/r_{200}$	−0.267	2.2σ	−0.298	2.5σ
O VI	Max $M_{\rm star}$	−0.247	1.9σ	−0.036	0.3σ
O VI	Isolated	−0.186	1.0σ	−0.322	1.8σ
Ne VIII	Min $d_{\rm proj}$	−0.088	0.3σ	−0.089	0.3σ
Ne VIII	Min $d_{\rm proj}/r_{200}$	−0.054	0.2σ	−0.085	0.3σ
Ne VIII	Max $M_{\rm star}$	−0.020	0.1σ	−0.062	0.2σ
Ne VIII	Isolated	−0.200	0.2σ	−0.200	0.2σ

Notes.
[a] Dependence of $N_{\rm OVI}$ and $N_{\rm NeVIII}$ on $d_{\rm proj}$ or $d_{\rm proj}/r_{200}$.
[b] Generalized Kendall correlation coefficient τ and corresponding significance.

smallest $d_{\rm proj}$. In addition, $N_{\rm OVI}$ correlates more strongly with r_{200}-normalized distance than with $d_{\rm proj}$.

The finding of a strong correlation between the observed O VI absorbers and the galaxies at the smallest $d_{\rm proj}/r_{200}$ is also supported by the bulk velocity distribution of the absorbers relative to the associated galaxies. Figure 5 shows the velocity dispersions (left panels) and escape velocity ($v_{\rm esc}$) normalized velocity dispersion (right) between the observed O VI and Ne VIII absorbers and the designated galaxies. We calculate $v_{\rm esc}$ based on the inferred dark halo mass for each galaxy in galaxy groups (see Section 2), assuming the Navarro–Frenk–White (NFW) profile (Navarro et al. 1996). While no significant difference is seen in the velocity dispersions between O VI and galaxies at either the smallest $d_{\rm proj}$ or smallest $d_{\rm proj}/r_{200}$, the $v_{\rm esc}$-normalized velocity dispersions are notably narrower for galaxies at the smallest $d_{\rm proj}/r_{200}$ (second panel on the right; showing a standard deviation of 0.40 ± 0.06) than those at the smallest $d_{\rm proj}$ (top-right panel; showing 0.56 ± 0.08). The difference is qualitatively consistent with the expectation that the observed absorbing gas is more closely connected to the galaxies at the smallest $d_{\rm proj}/r_{200}$. In the subsequent analysis, we adopt the galaxy at the smallest r_{200}-normalized $d_{\rm proj}$ as the counterpart of the absorber to explore the connection between galaxies and absorption properties. Here, we ignore the potential impact on O VI or Ne VIII due to nearby environments (e.g., Dutta et al. 2021), which will be investigated in future CUBS works.

3.2. Spatial Properties of the Warm-hot CGM Probed by O VI and Ne VIII

By designating the galaxies at the smallest $d_{\rm proj}/r_{200}$ as the primary driver of the observed line-of-sight absorption properties in a group environment, we proceed with a joint study of the spatial properties of the warm-hot CGM using the full sample of isolated galaxies and galaxy groups. Using this full sample, we show the spatial profiles of $N_{\rm OVI}$ and $N_{\rm NeVIII}$ versus $d_{\rm proj}/r_{200}$ in Figure 6. On average, both $N_{\rm OVI}$ and $N_{\rm NeVIII}$ exhibit a general decline with increasing distance. Specifically, the detected O VI systems exhibit high column densities of $\log N/{\rm cm}^{-2}\gtrsim 14.5$ at $<0.5\,r_{200}$, together with two nondetections among six sightlines showing 2σ upper limits of $\log N/{\rm cm}^{-2}\lesssim 13.5$ within r_{200} (Figure 6). In the outskirts at $\gtrsim 2r_{200}$, the overall strengths of detected O VI with column densities of $\log N/{\rm cm}^{-2}\approx 13.5$–$14.0$ are sufficiently weak in comparison to the sensitivity of the data that a large fraction of sightlines show nondetections with a limiting column density of $\log N/{\rm cm}^{-2}\lesssim 13.7$.

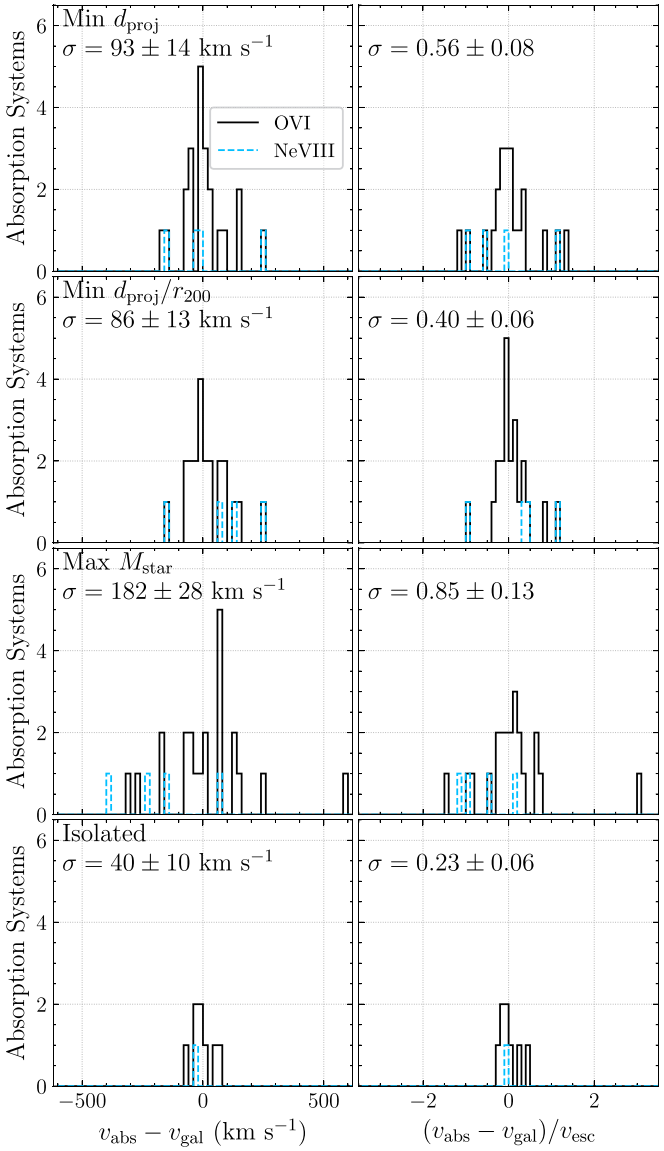

Figure 5. Observed line-of-sight velocity distribution of O VI and Ne VIII absorbers in the galaxy rest frame. Solid histograms represent the O VI absorbers, while dashed histograms represent the Ne VIII absorbers. Galaxies are selected following the same criteria described in Figures 4 and A1. The right panels display escape velocity ($v_{\rm esc}$) normalized velocity dispersion. The standard deviation (σ) of the O VI velocity distribution is marked in the top-right corner of each panel. The narrower $v_{\rm esc}$-normalized velocity dispersion in the right panel in the second row suggests a tighter kinematic connection between the O VI absorbers and the galaxies at the smallest $d_{\rm proj}/r_{200}$ in a group environment. Similar to the column density profiles displayed in Figure A1, the small number of Ne VIII absorbers detected in our search provides little distinction for their galaxy hosts.

We determine the covering fractions of O VI- and Ne VIII-absorbing gas above a column density threshold, N_0, versus the projected distance. These are presented at the top of each panel in Figure 6, which shows that the gas covering fraction also decreases with increasing distance. For O VI, the adopted threshold for calculating the covering fraction is $\log N_0/{\rm cm}^{-2}=13.7$, which is larger than 95% of the upper limits reported for the sample. It allows us to include the majority of the sample for the covering fraction calculation.

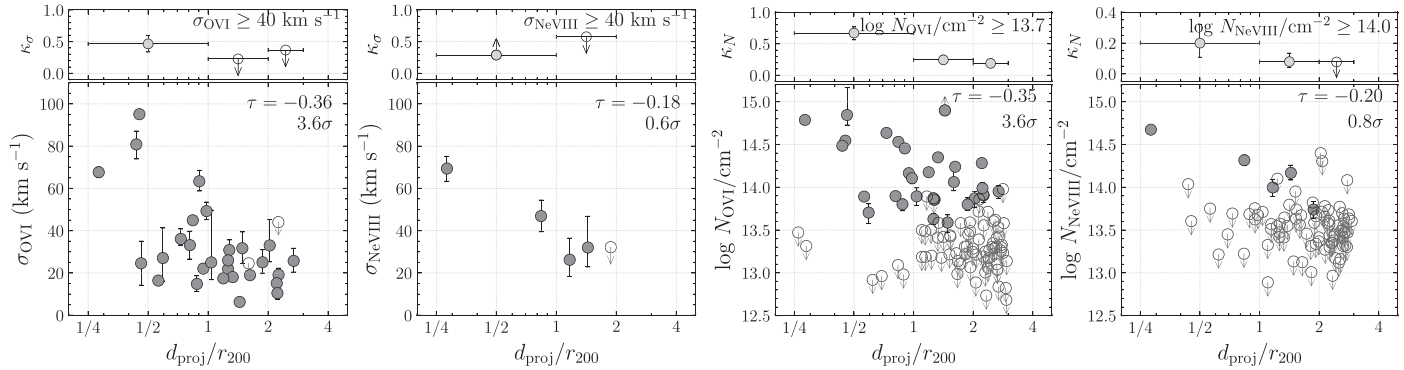

Figure 6. Spatial profiles of column densities and velocity dispersion for O VI and Ne VIII, together with the estimated covering fraction of high column density absorption systems with $\log N/{\rm cm}^{-2} \geqslant 13.7$ and 14.0 for O VI and Ne VIII, respectively, at the top. For velocity dispersions, the covering fractions are calculated for broad features with $\sigma_v \geqslant 40$ km s^{-1}.

The covering fraction is calculated assuming a binomial distribution applied to small samples (see, e.g., Gehrels 1986). Within r_{200}, the covering fraction of O VI absorbers with $\log N_{\rm OVI}/{\rm cm}^{-2} \geqslant 13.7$ is $\kappa_N = 67 \pm 10\%$ (median and 1σ uncertainty), and declines to $25 \pm 7\%$ and $19 \pm 6\%$ at $2r_{200}$ and $3r_{200}$, respectively.

For Ne VIII, the column density profile resembles that of O VI, exhibiting higher column densities within r_{200}. However, significantly fewer detections are found and the data are not sufficiently sensitive for detecting Ne VIII with $\log N/{\rm cm}^{-2} \lesssim 14$. Adopting a threshold of $\log N_0/{\rm cm}^{-2} = 14.0$, we estimate a covering fraction of $\kappa_N = 20^{+12}_{-9}\%$ for Ne VIII-bearing gas within r_{200}, which declines to $4^{+3}_{-2}\%$ at 1–3r_{200}. While the detected Ne VIII sample is small, the decline in the covering fraction is significant. To obtain a better constraint of the covering fraction, we combine the CUBS sample with literature samples, which will be presented in Section 5.2.

As described in Section 2.3, the line-of-sight velocity dispersion σ_v can serve as a tracer of the intra-halo kinematics, when the feature is broad $\geqslant$40 km s^{-1}. Figure 6 shows that there is a general decline of σ_v from inner halos to the outskirts for both O VI and Ne VIII. In particular, broad Ne VIII features are all associated with broad O VI features. All six broad O VI and two Ne VIII absorbers are projected within r_{200}, leading to a covering fraction of $\kappa_\sigma = 46 \pm 13\%$ for these broad absorbers and $\kappa_\sigma > 29\%$ at the 2σ level of significance for O VI and Ne VIII, respectively. Beyond r_{200}, we can only place a 2σ upper limit of 16% and 58% for broad O VI and Ne VIII absorbers, respectively. The difference in the covering fraction of broad O VI absorbers between within and beyond r_{200} is statistically significant (at the level of $\approx 2\,\sigma$), suggesting that the gas kinematics is more complicated at $d_{\rm proj} < r_{200}$.

4. Dependence of the Warm-hot CGM on Galaxy Properties

The new CUBS-midz sample includes isolated galaxies and galaxy groups containing two to 21 member galaxies. The analysis presented in Section 3 shows that in the presence of neighbors, the galaxy at the smallest $d_{\rm proj}/r_{200}$ is physically most connected to the absorbers identified along the QSO sightlines (see Section 3). In this section, we explore how the warm-hot CGM probed by O VI and Ne VIII correlates with galaxy properties. In particular, we focus on its relation to $M_{\rm star}$ and SFR, which characterizes a galaxy's star formation history.

For literature samples, we adopt the reported total ion column densities when these measurements are available. When the best-fit Voigt profile parameters are reported for individual components, we compute a total column density by summing all components based on the Voigt profile fitting results. For nondetections, we compute the corresponding 2σ limits based on the reported upper limits for all samples. Finally, we calculate a velocity dispersion for each absorber in the literature samples based on the reported Voigt profile results, including the J17, COS-Halos, and COS-LRG samples. For the literature samples, the adopted column densities and calculated velocity dispersions are also included in Figure 3 for comparisons.

Combining the CUBS-midz and literature samples leads to a joint sample of galaxies that span a range in $M_{\rm star}$ from $\log M_{\rm star}/M_\odot \approx$ 8–11.5 over a redshift range from $z \approx 0.1$–1.0. To ensure a consistent treatment of the absorber and galaxy association, we examine the public samples in search of possible neighbors and identify the galaxies at the smallest $d_{\rm proj}/r_{200}$ as the designated galaxies associated with the reported O VI or Ne VIII absorbers. Virial radii are adopted from each sample directly for the J17 and COS-LRG samples (Zahedy et al. 2019) because the calculation methods are the same. We recalculate the virial radius for the COS-Halos sample (Werk et al. 2013). However, because of inhomogeneous survey limits between the literature samples, discrepancies remain in characterizing the galaxy environments between the CUBS and these literature samples. The impact due to variations in survey depth will be discussed when combining these samples for further studies.

4.1. Dependence of O VI- and Ne VIII-bearing Gas on the Stellar Mass

In Figure 7, we examine the dependence of $N_{\rm OVI}$ and $N_{\rm NeVIII}$ on the stellar mass. High-$N_{\rm OVI}$ absorbers with $\log N/{\rm cm}^{-2} \gtrsim 14.5$ are found surrounding galaxies of $\log M_{\rm star}/M_\odot \approx$ 9.5–10.5, which is consistent with previous studies (e.g., Werk et al. 2014; Zahedy et al. 2019; Tchernyshyov et al. 2022). For a given $M_{\rm star}$, the observed $N_{\rm OVI}$ ranges from the 2σ upper limits of $\log N/{\rm cm}^{-2} \lesssim 13.0$ for nondetections to $\log N/{\rm cm}^{-2} \gtrsim 14.0$ for measurements, which is driven by the radial decline shown in Figure 6. For comparison, we plot the predicted $N_{\rm OVI}$ from semi-analytical CGM models for star-forming galaxies at $z = 0.2$ and at $0.2r_{200}$ and $1.0r_{200}$ from (Qu & Bregman 2018, hereafter, QB18; see also Section 5.4). The predicted $N_{\rm OVI}$ for galaxies of different

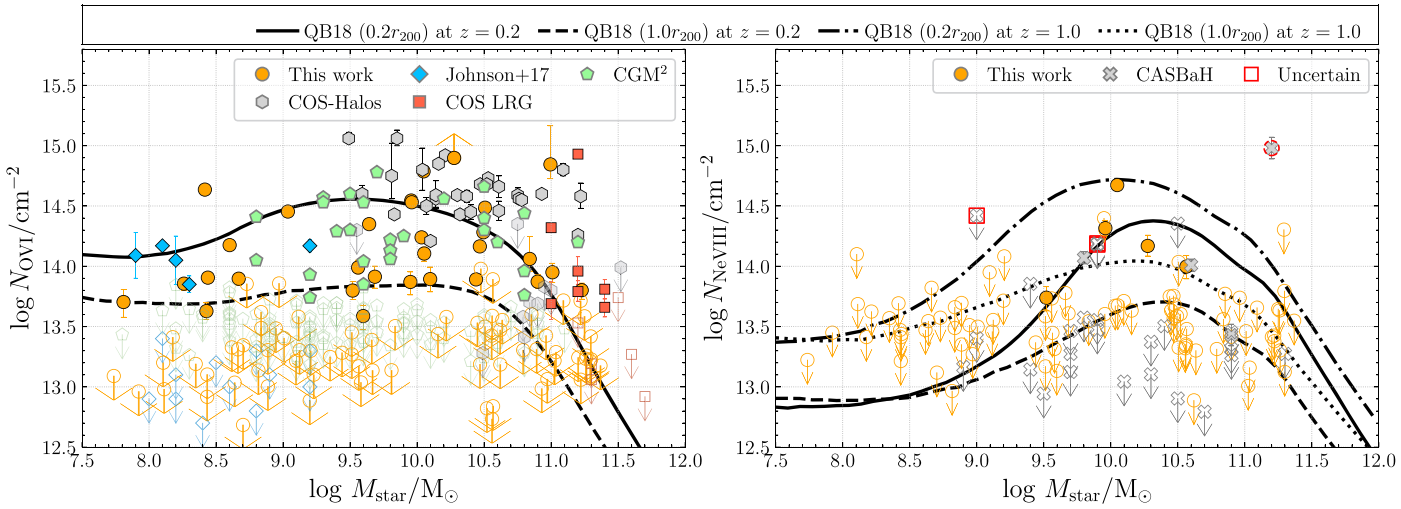

Figure 7. Dependence of ion column density on $M_{\rm star}$ for O VI (left panel) and Ne VIII (right panel). Recall that in the presence of neighbors, we associate the observed line-of-sight absorption properties with the galaxy at the smallest $d_{\rm proj}/r_{200}$. Measurements from the literature, including COS-Halos (Werk et al. 2013), J17, COS-LRG (Zahedy et al. 2019), CASBaH (Burchett et al. 2019), and CGM^2 (Tchernyshyov et al. 2022) are also included. In these samples, the maximum $d_{\rm proj}/r_{200}$ are all smaller than 3. Theoretical models adopted from QB18 are plotted for comparisons (curves). Both observations and theoretical models indicate that the observed ion abundances peak at $\sim 10^{10}\,M_\odot$ for both O VI and Ne VIII. For the CASBaH Ne VIII sample, reported Ne VIII systems with significant contaminations in Burchett et al. (2019) are marked as uncertain systems in red squares (see the text for details). One outlying strong Ne VIII absorber (circled in red) near a massive galaxy of $\log M_{\rm star}/M_\odot = 11.2$ containing an AGN is likely associated with AGN outflows (Tripp et al. 2011; Burchett et al. 2019).

$M_{\rm star}$ differs by a factor of 5–10 between projected distances of $0.2r_{200}$ and $1.0r_{200}$. The large scatter implies that the O VI-bearing gas may exhibit different radial distributions on different mass scales. We will explore this further in the following section.

For Ne VIII, we include the CASBaH sample in the analysis. However, we have to first construct a uniform sample by adopting the same identification criteria stated in Section 2.3. For absorption features with significant contamination from interlopers, we consider the reported $N_{\rm NeVIII}$ as upper limits. This leaves four of the nine Ne VIII absorbers reported by Burchett et al. (2019) as detections and the remaining five as nondetections (red squares in Figure 7). The four confirmed systems are PHL1377: 221_15, PG1206 + 459: 178_9, and PG1407 + 265: 245_62, and FBQS0751 + 0919: 124_25 (see Figure 2 of Burchett et al. 2019). In addition, we recalculate the halo size for the CASBaH galaxies using their reported $M_{\rm star}$ and the method described in Section 2.1. This is necessary because of the significant difference in the adopted SMHM relations (see the details in Wijers et al. 2024).

As shown in Figure 7, Ne VIII features are primarily detected around galaxies with $\log M_{\rm star}/M_\odot \approx 9.5$–$11.0$. We find that the strongest Ne VIII features occur near galaxies of $\log M_{\rm star}/M_\odot \approx 10$, similar to O VI. One outlying system with $\log N_{\rm NeVIII}/{\rm cm}^{-2} = 14.98 \pm 0.09$ in the CASBaH sample is likely associated with outflows from a massive post-starburst galaxy of $\log M_{\rm star}/M_\odot = 11.2$ at $z = 0.93$. This galaxy exhibits spectral features that are indicative of the presence of an active galactic nucleus (AGN; Tripp et al. 2011). It is different from typical galaxies in the combined sample, but it is still included in the following analyses.

Next, we examine how the line-of-sight velocity dispersion, σ_v, depends on $M_{\rm star}$, which may shed light on the ionization mechanisms of the warm-hot CGM. In PIE models, the typical density of O VI is $\approx 10^{-4}\,{\rm cm}^{-3}$ (e.g., Oppenheimer & Schaye 2013; Stern et al. 2018, hereafter S18), with an equilibrium temperature of $\log T/{\rm K} \approx 4.5$ and a velocity dispersion of $\sigma_v \approx 4\,{\rm km\,s}^{-1}$ due to thermal motions. In contrast, under a CIE assumption, the ionization fraction of O VI peaks at a temperature of $\log T/{\rm K} \approx 5.5$ with an anticipated thermal broadening of $\sigma_v \approx 12.8\,{\rm km\,s}^{-1}$.

In Figure 8, the velocity dispersion of O VI absorbers spans a wide range from $\approx$5–120 km s^{-1}, while Ne VIII absorbers exhibit a minimum $\sigma_v \approx 20$–$30\,{\rm km\,s}^{-1}$. We first note that the narrow O VI features with $\sigma_v \approx 5$–$10\,{\rm km\,s}^{-1}$ are likely photoionized or out of equilibrium (e.g., Oppenheimer & Schaye 2013). On the other hand, the broad components with $\sigma_v \geqslant 40\,{\rm km\,s}^{-1}$ are preferentially seen surrounding galaxies of $\log M_{\rm star}/M_\odot > 9$ for both O VI and Ne VIII, and the majority of broad features are detected around galaxies of $\log M_{\rm star}/M_\odot \approx 10$–$11$. For these massive galaxies, the observed gas velocity dispersion exhibits a large scatter similar to what is seen in the column density. We attribute the observed large scatter to the complex gas kinematics at small $d_{\rm proj}/r_{200}$ (Figure 6).

4.2. Dependence of O VI-bearing Gas on Galaxy Star Formation History

Next, we examine whether the radial profiles of O VI column density and kinematics depend on a galaxy's star formation history by dividing the CUBS galaxy sample into subsamples in the $M_{\rm star}$ versus SFR parameter space (Figure 2). These include (i) a low-mass dwarf galaxy sample of 29 galaxies with $7.5 \lesssim \log M_{\rm star}/M_\odot \leqslant 9.0$ and a median mass of $\langle \log M_{\rm star}/M_\odot \rangle = 8.6$; (ii) a sub-$L_*$ sample of 34 galaxies with $9.0 < \log M_{\rm star}/M_\odot \leqslant 10.3$ and a median of $\langle \log M_{\rm star}/M_\odot \rangle = 9.6$; (iii) a massive, star-forming sample of 12 galaxies with $\log M_{\rm star}/M_\odot > 10.3$ and a median of $\langle \log M_{\rm star}/M_\odot \rangle = 10.7 \pm 0.3$; and (iv) a massive quiescent sample of 29 galaxies with $\log M_{\rm star}/M_\odot > 10.3$ and a median of $\langle \log M_{\rm star}/M_\odot \rangle = 10.9 \pm 0.3$. Both the low-mass dwarf and the sub-L_* subsamples are predominantly star-forming galaxies with $\log {\rm sSFR/yr}^{-1} > -10.3$, while massive galaxies with an SFR $> 0.2\,M_\odot\,{\rm yr}^{-1}$ are considered star-forming and quiescent otherwise. This SFR threshold splits

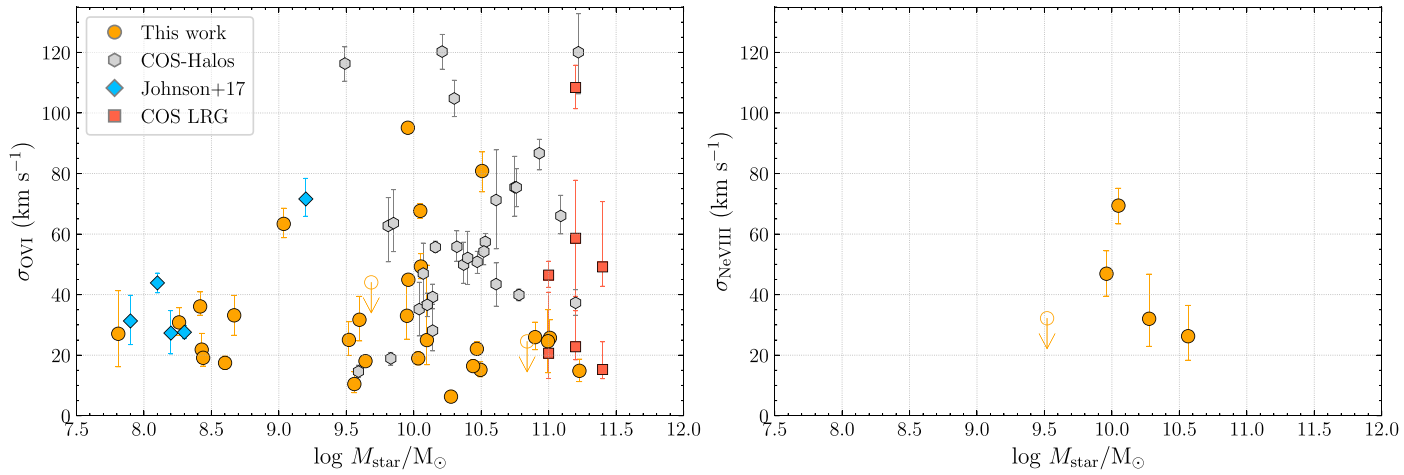

Figure 8. The velocity dispersion dependence on the stellar mass of the galaxy with the minimal $d_{\rm proj}/r_{200}$ for O VI (left panel) and Ne VIII (right panel). Broad O VI absorption features of $\sigma_v \geqslant 40$ km s^{-1} are detected at $\log M_{\rm star}/M_\odot \gtrsim 9.0$, while narrow features are found for all stellar masses.

massive galaxies to have roughly equal numbers in each subsample together with literature samples.

Figure 9 shows the radial profiles of column density and velocity dispersion for these subsamples, i.e., dwarf, sub-L^*, massive star-forming, and massive quiescent galaxies from left to right, respectively. Here, we also include the COS-Halos (Werk et al. 2013), J17, and COS-LRG samples (Zahedy et al. 2019) for improved statistics but leave out CGM^2 because the SFRs their galaxies and velocity dispersions of absorbers are not available (Tchernyshyov et al. 2022).

The differences in the O VI column density profiles are significant between these four subsamples. Strong O VI absorbers with $\log N/{\rm cm}^{-2} \gtrsim 14.5$ preferentially occur in the inner halo of sub-L^* and massive star-forming galaxies, and the decline of $N_{\rm OVI}$ with increasing $d_{\rm proj}/r_{200}$ is correspondingly significant in these two subsamples. This behavior explains that the on average higher O VI column density observed in the COS-Halos sample relative to the others may be understood as due to the QSO sightlines probing primarily the inner halo of galaxies with $\log M_{\rm star}/M_\odot \approx 10$.

We adopt the generalized Kendall correlation coefficient τ (Figure 9) to quantify the significance of the anticorrelation in the presence of upper limits and find a significance level of $>4\sigma$ for the sub-L^* and massive star-forming samples. In contrast, the dwarf and massive quiescent subsamples exhibit weaker correlations between $N_{\rm OVI}$ and $d_{\rm proj}/r_{200}$.

To investigate this difference quantitatively, we perform an analysis under a Bayesian framework to obtain a best-fit radial profile of both ion column density and covering fraction for each subsample. This two-component model is developed to account for the possible clumpy nature of the O VI-bearing gas (see also Huang et al. 2021), and motivated by the observation that a single continuous probability distribution of $N_{\rm OVI}$ cannot simultaneously reproduce the observed high-$N_{\rm OVI}$ systems and nondetections within r_{200} (Section 3.2 and Figure 6). Instead, the difference between detections and nondetections can be explained by a nonunity covering fraction, ϵ. We note that ϵ is a theoretical parameter that depicts the presence or absence of O VI gas, while κ is an empirical number that is affected by the sensitivity of the data, and therefore, is only meaningful with an associated column density threshold. In practice, the modeling of ϵ may be affected by the detection limits, when QSO spectra have low-S/N ratios. Here, we note the spectral S/N is sufficient to characterize ϵ for O VI in the CUBS program.

The two-component model is implemented by combining the spatial variations of ϵ and $N_{\rm OVI}$ as a function of $d_{\rm proj}/r_{200}$. We adopt a power-law radial profile for the expected O VI column density $\hat{N}$ of

$$\hat{N}(x) = \hat{N}_0 x^{-\alpha}, \tag{4}$$

where $x = d_{\rm proj}/r_{200}$, $\hat{N}_0$ is the expected O VI column density at r_{200} and α is the slope. The power law is selected because detected column densities do not exhibit a sharp decline, and it is also typically adopted in such modeling (e.g., Chen et al. 1998; Huang et al. 2021). Here, we only fit data with x in the range of 0.1–3, so we can ignore the singularity at $x = 0$ for the power law.

For the covering fraction, we assume a modified exponential decline of

$$\epsilon(x) = {\rm Min}\left[1,\ \epsilon_0 \exp\left(-\left(\frac{x}{x_0}\right)^\beta\right)\right], \tag{5}$$

where x_0 is the r_{200}-normalized scale radius of the exponential model, β is the free index regulating the speed of decline, and ϵ_0 is the covering fraction at the galaxy center. Because the mathematical form as given allows ϵ_0 to be larger than unity, we impose a ceiling at $\epsilon = 1$. This modified exponential function is motivated by the sharp decline in the covering fraction (Figure 6), which has also been seen for Mg II-bearing gas (Huang et al. 2021; Schroetter et al. 2021). In our model, if $\beta > 1$, then ϵ would decline faster than an exponential function. Therefore, this modified exponential function provides the flexibility to capture different degrees of declining rate.

The likelihood of producing an observed data set D that contains n measurements, m nondetections, and l saturated lines under the two-population model M consisting of parameters $\hat{N}_0$, α, ϵ_0, x_0, and β is the joint product of (i) the probability of measuring N_i for an expected $\hat{N}$ and (ii) the probability of the model values occurring within the range of the allowed upper or lower limits by the data. We construct a likelihood function

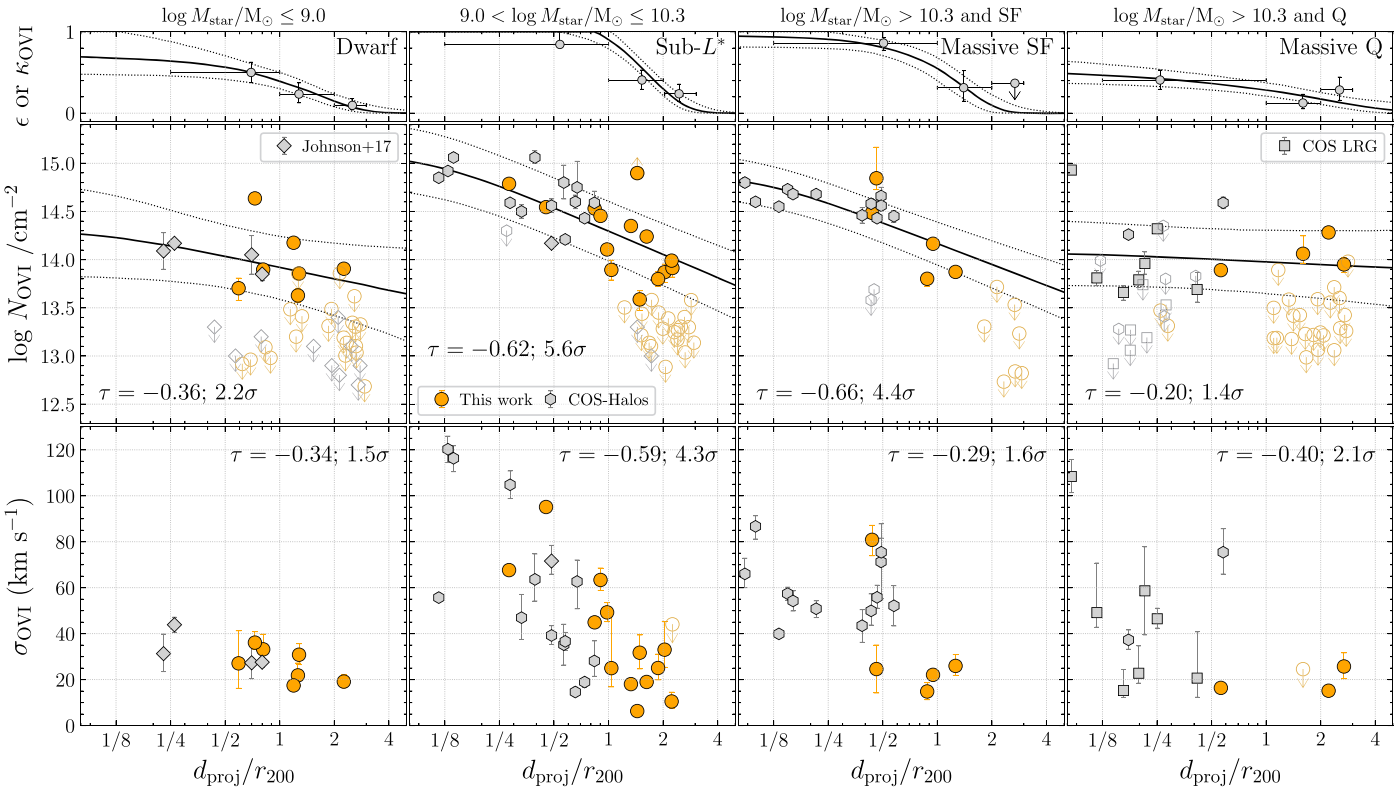

Figure 9. Radial profiles of column density $N_{\rm OVI}$, covering fraction ϵ, and velocity dispersion $\sigma_{\rm OVI}$ of O VI-bearing gas for low-mass dwarf, sub-L^*, massive star-forming, and massive quiescent galaxies from the left to right columns, respectively. In this plot, we include the literature samples in the analysis, the J17 dwarf sample (diamonds), COS-Halos (hexagons; Werk et al. 2013), and COS-LRG (squares; Zahedy et al. 2019). We calculate Kendall's rank order coefficient τ to quantify the significance of the correlation, which is listed in each panel. We fit the column density radial profile using a two-component model, including both the radial profiles of the column density (the middle row) and rate of incidence (the top row) to account for the clumpiness of the O VI gas (see the text for details). The solid line in each panel shows the best-fit model, while the dotted lines represent the 1σ uncertainties. Circles in the top panels represent the empirical covering fraction measurements obtained based on a threshold of $\log N/{\rm cm}^{-2} \geqslant 13.7$. The sub-$L^*$ and massive star-forming galaxy samples exhibit steeper declines with power-law slopes of $\approx$0.9, while the massive quiescent galaxy sample shows a flatter profile, consistent with a zero slope.

following this joint probability,

$$\mathcal{L}(D|M) \propto \prod_{i=1}^{n} \frac{\epsilon}{\sigma\sqrt{2\pi}} \exp\left(-\frac{(\log N_i - \log \hat{N})^2}{2\sigma^2}\right) \times \prod_{i=1}^{m} \left[\left(\frac{\epsilon}{\sigma_{\rm p}\sqrt{2\pi}} \int_{-\infty}^{\log N_i^u} \exp\left(-\frac{(y - \log \hat{N})^2}{2\sigma_{\rm p}^2}\right) dy\right) + (1-\epsilon)\right] \times \prod_{i=1}^{l} \frac{\epsilon}{\sigma_{\rm p}\sqrt{2\pi}} \int_{\log N_i^l}^{+\infty} \exp\left(-\frac{(y - \log \hat{N})^2}{2\sigma_{\rm p}^2}\right) dy, \quad (6)$$

where $y = \log N/{\rm cm}^{-2}$, $\sigma^2 = \sigma_i^2 + \sigma_{\rm p}^2$, with σ_i representing the measurement uncertainty and $\sigma_{\rm p}$ representing the intrinsic scatter. The symbols N_i, N_i^u, and N_i^l represent measurements, 95% upper limits in the case of nondetections, and 95% lower limits in the case of saturated lines, respectively. The term $(1-\epsilon)$ associated with upper limits accounts for the probability that the nondetection is from the region without O VI-bearing gas.

We assume a uniform prior and construct the posteriors of individual model parameters $\log \hat{N}_0$, α, ϵ_0, x_0, β, and $\sigma_{\rm p}$ based on Markov Chain Monte Carlo, which is implemented using the `emcee` package (Foreman-Mackey et al. 2013). The best-fit parameters are summarized in Table 2. The median and 68% interval of the best-fit model are presented as solid and dashed lines in Figure 9.

Figure 9 and Table 2 show that while the sub-L^* and massive star-forming subsamples share a similar power-law slope for the O VI-bearing gas (0.86 ± 0.19 versus $0.75^{+0.19}_{-0.18}$), the massive quiescent subsample exhibits a flatter slope of $0.10^{+0.24}_{-0.22}$, respectively. The dwarf galaxy sample shows a flatter slope of $0.39^{+0.44}_{-0.39}$, but its difference from sub-L^* and massive star-forming galaxies is limited by the small sample size. Within a similar mass range, star-forming galaxies exhibit a steeper slope than the quiescent ones at a significance level of $\approx 1.6\,\sigma$. This implies a fundamental difference in the spatial distribution of O VI between star-forming and quiescent galaxies.

We also compare the observed covering fraction at a threshold of $\log N_{\rm OVI}/{\rm cm}^{-2} = 13.7$, κ, with the model-predicted covering fraction, ϵ, in Figure 9. Similar to the column density profile, sub-L^* and massive star-forming galaxies exhibit covering fractions consistent with unity at $\lesssim 0.5 r_{200}$ and declining to $\lesssim$20% beyond $2r_{200}$. At the same time, dwarf galaxies exhibit a maximum covering fraction of $\approx$60% at 0.5–1.0r_{200}. The decline of covering fractions is significant for the three star-forming galaxy samples, with $\beta \approx 2$. The scale radius (r_0) is about $1.5r_{200}$, suggesting an enhancement of the O VI-bearing gas within $\approx r_{200}$, due to the nearby star-forming galaxies.

In contrast, the massive quiescent galaxy sample exhibits a roughly constant covering fraction of $\approx$30% within $3r_{200}$. The best-fit $\beta = 0.7^{+1.2}_{-0.4}$ is smaller than the three star-forming

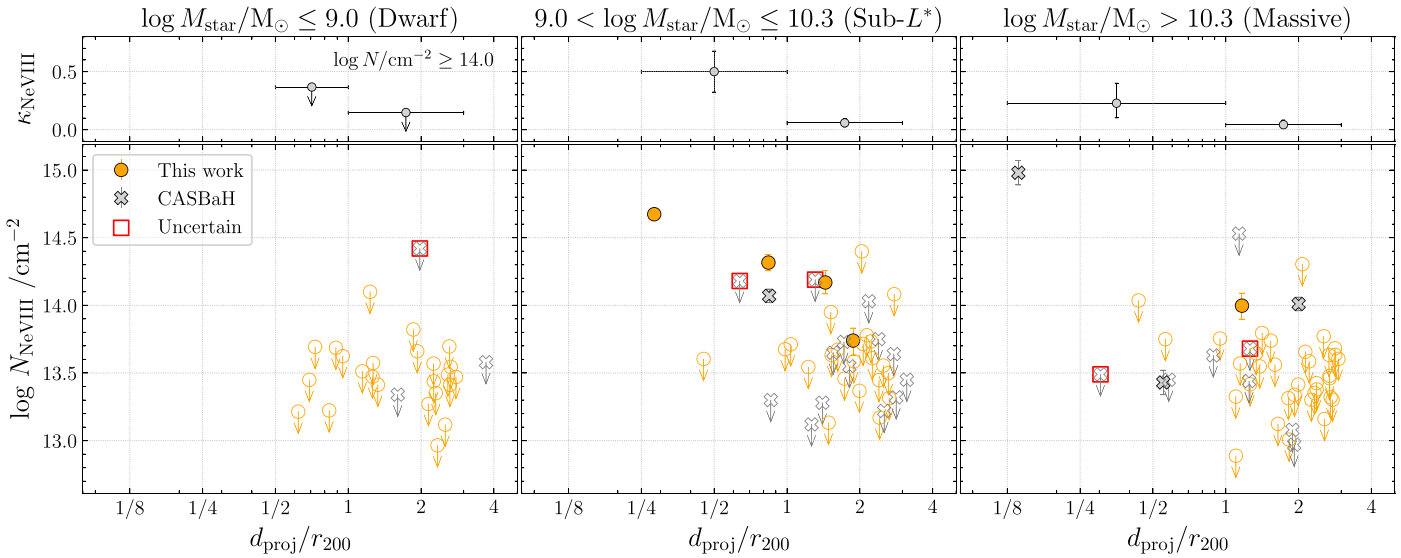

Figure 10. The radial dependence of Ne VIII column density and covering fraction for dwarf, sub-L^*, and massive galaxies. The CASBaH sample is also plotted (crosses) with uncertain/contaminated detections marked with a red square (see the details in Section 4.1). The covering fractions are calculated for a threshold of $\log N/{\rm cm}^{-2} \geqslant 14.0$. High column density Ne VIII systems are more concentrated in sub-L^* galaxy halos.

Table 2
The Best-fit Models of the Radial Profiles of the Column Density for Different Galaxy Samples

Sample	$\log N_0/{\rm cm}^{-2}$	α	ϵ_0	x_0 (r_{200})	β	$\sigma_{\rm p}$
Dwarf	$13.93^{+0.12}_{-0.13}$	$0.39^{+0.44}_{-0.39}$	$0.63^{+0.46}_{-0.21}$	$1.5^{+0.5}_{-0.7}$	$1.7^{+1.4}_{-0.9}$	$0.33^{+0.10}_{-0.07}$
Sub-L^*	14.32 ± 0.07	0.86 ± 0.19	[0.95, 2.0][a]	1.6 ± 0.3	$2.1^{+0.9}_{-0.7}$	$0.32^{+0.06}_{-0.05}$
Massive SF	14.20 ± 0.09	0.74 ± 0.21	$1.04^{+0.43}_{-0.17}$	$1.2^{+0.4}_{-0.3}$	$2.0^{+1.2}_{-0.9}$	$0.21^{+0.06}_{-0.04}$
Massive Q	$13.97^{+0.13}_{-0.12}$	$0.12^{+0.23}_{-0.25}$	$0.60^{+0.35}_{-0.20}$	[0.1, 3.0][b]	$0.8^{+1.0}_{-0.4}$	0.3 (fixed)[c]

Notes.
[a] For sub-L^* galaxies, the data do not provide distinguishing power a $\epsilon_0 > 1$ because of a high covering fraction of O VI-bearing gas in the inner halo. The upper bound of 2.0 is the fixed boundary for ϵ_0.
[b] For massive quiescent galaxies, a roughly flat covering fraction cannot distinguish x_0 within the allowed range of [0.1, 3.0].
[c] In the massive quiescent sample, $\sigma_{\rm p} > 0.3$ dex cannot be distinguished by the data, so we fixed $\sigma_{\rm p} = 0.3$ dex, similar to the other subsamples.

samples ≈2.0, suggesting a shallower decline. In this case, the scale radius r_0 is unconstrained because of the roughly constant covering fraction.

The difference between star-forming and quiescent galaxy CGM has also been seen in low ions. For example, the rest-frame absorption EW of Mg II shows a power-law slope of 1.03 ± 0.22 for the star-forming sample, while the passive galaxy sample exhibits a slope of 0.12 ± 0.24 (Huang et al. 2021). The cool and warm-hot gas in the CGM both exhibit concentrations in the inner halo of star-forming galaxies, compared to passive galaxies. However, the covering fraction of ≈50% for high column density absorbers occurs at 1–1.5r_{200} for O VI, while this radius is 0.5r_{200} for Mg II, indicating changing ionization states of the gas toward halo outskirts.

Figure 9 also shows a larger velocity dispersion within r_{200} than in the outskirts for all four subsamples. Here, we adopt the generalized Kendall's τ test to quantify the degree of anticorrelations for these samples. The sub-L^* sample exhibits a significant decline (4.3σ) from the maximum of 120 km s^{-1} within 0.2r_{200} to ≈20 km s^{-1} at 1–2r_{200}, with all broad features ($\geqslant$40 km s^{-1}) projected within the virial radius. Anticorrelations are observed for the other three subsamples, but less significant $\lesssim 2\sigma$. In addition, we notice almost all O VI features are broad within 0.5r_{200} for sub-L^* and massive star-forming galaxies, while there are also narrow features within 0.5r_{200} for massive quiescent galaxies. The joint observations of enhanced $N_{\rm OVI}$ and broader σ_v at $\lesssim$0.5r_{200} around star-forming galaxies support that these high-$N_{\rm OVI}$ at small $d_{\rm proj}/r_{200}$ absorbers do indeed originate in the galaxy halo, rather than appearing by projection (see Ho et al. 2021).

4.3. Dependence of Ne VIII-bearing Gas on Galaxy Properties

Similar to O VI, we consider the dependence of Ne VIII profiles on galaxy properties. For Ne VIII, limited by the small number of detections, we only divided the uniform combined sample (Section 4.1) into three subsamples based on $M_{\rm star}$, separated at $\log M_{\rm star}/M_\odot = 9.0$ and 10.3. In Figure 10, we present radial profiles of $N_{\rm NeVIII}$ as a function of $d_{\rm proj}/r_{200}$ for these three subsamples.

Although the nine detected Ne VIII absorption systems exhibit a declining trend with increasing distance, the radial profile of $N_{\rm NeVIII}$ cannot be quantitatively modeled using the two-component model because of the small number of detections. Here, we calculate the covering fractions for the high column density Ne VIII systems of $\log N/{\rm cm}^{-2} \geqslant 14.0$ for different galaxies. There is no robust detection of Ne VIII in halos around dwarf galaxies, leading to 2σ upper limits in covering fractions of 36% and 15% within and beyond r_{200}, respectively. For sub-L^* galaxies, the covering fraction exhibits a significant decline from $50 \pm 17\%$ within r_{200} to $6 \pm 3\%$ at

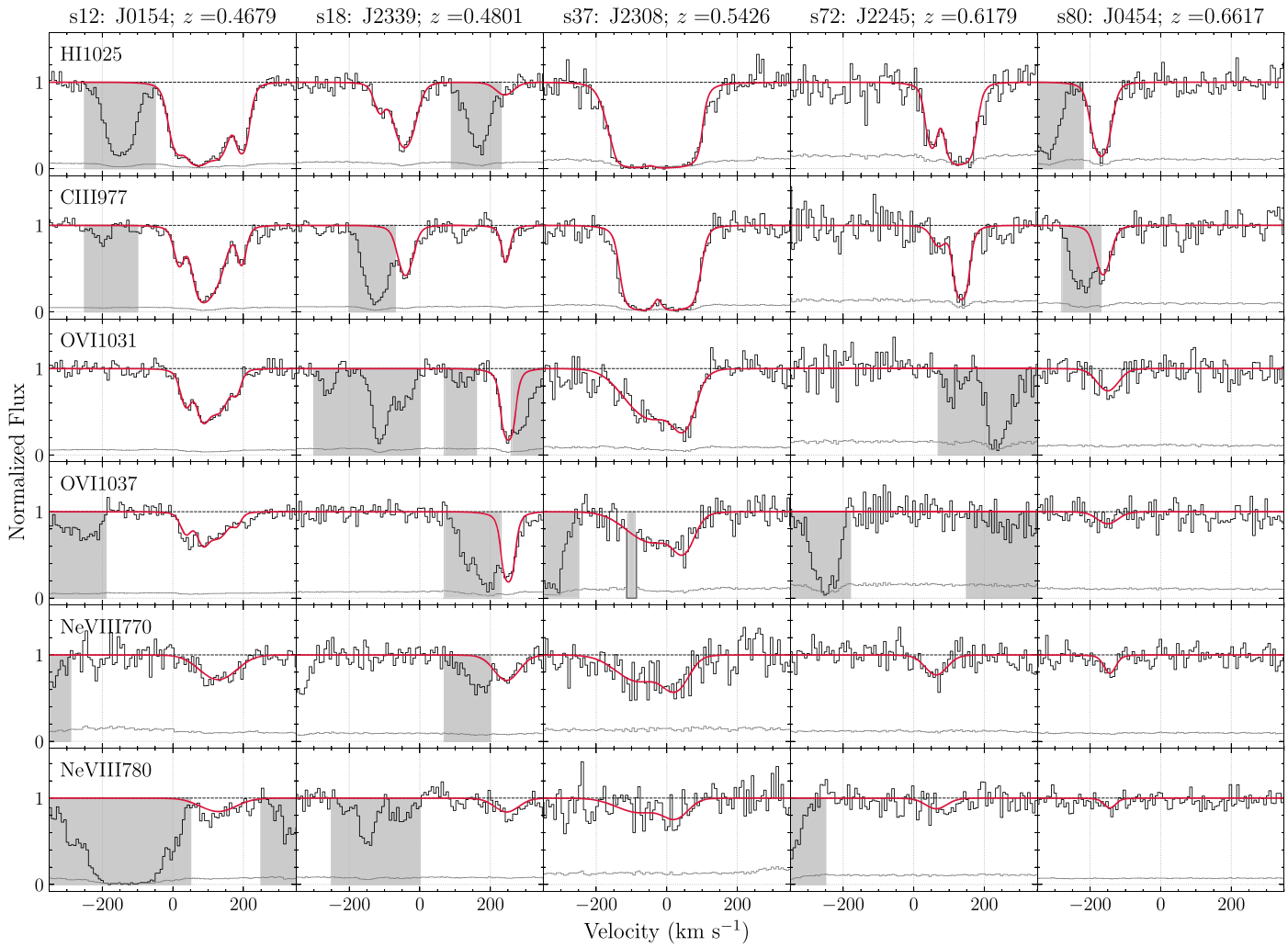

Figure 11. Absorption properties of all five newly discovered Ne VIII systems in the CUBS-midz sample, together with associated low-ionization transitions including Lyβ, C III λ977, O VI $\lambda\lambda$1031, 1037, and Ne VIII $\lambda\lambda$770, 780. Zero velocity represents the galaxy at the smallest $d_{\rm proj}/r_{200}$. The red lines denote the best-fit models obtained from the Voigt profile fitting for each transition. The gray-shaded regions mark contaminating features or bad pixels.

1–3r_{200}. In massive halos, the covering fraction is 23^{+17}_{-12}% within r_{200}. However, the only high column density Ne VIII is associated with a post-starburst AGN-host galaxy. Ignoring this outlier, the covering fraction is <41% within r_{200}. Beyond r_{200}, only two systems are detected with $\log N/{\rm cm}^{-2} \approx 14.0$, which leads to a low covering fraction of 4^{+4}_{-2}%. The difference in Ne VIII covering fractions between sub-L^* and massive galaxy halos suggests that sub-L^* halos contain more concentrated Ne VIII-absorbing gas, similar to O VI.

5. Discussion

Combining the CUBS-midz sample with previously published literature samples, we have demonstrated that galaxies with different star formation histories, determined according to $M_{\rm star}$ and SFR, exhibit different radial profiles of O VI and Ne VIII absorption properties (N and σ_v). In this section, we first examine the galaxy environments of the five new Ne VIII absorbers discovered in our survey and then discuss the implications of our findings for the warm-hot CGM, including its spatial distribution, total mass, and possible origins in halos of different masses.

5.1. Notes on Individual Ne VIII Absorbers

As described in Section 2.3, the detected Ne VIII absorbers are identified based on a matched doublet ratio without significant contamination and with both doublet components detected at $\gtrsim 2\sigma$. All five detected Ne VIII absorbers also exhibit low-ionization species over a similar velocity range (e.g., H I and C III), as shown in Figure 11. Four of five systems have detectable O VI features, while one system shows a 2σ upper limit of $\log N/{\rm cm}^{-2} < 13.9$.

These newly discovered Ne VIII absorbers are found in a range of galactic environments (Figure 12). In particular, the strongest Ne VIII of $\log N/{\rm cm}^{-2} = 14.67 \pm 0.05$ is detected in the inner halo ($d_{\rm proj} \approx 30$ kpc) of an isolated star-forming disk galaxy with $\log M_{\rm star}/M_\odot = 10.0 \pm 0.1$ (i.e., system s37) that produces an LLS system (Chen et al. 2020; Zahedy et al. 2021). The remaining Ne VIII absorbers are detected in galaxy groups with the number of members ranging between five and 21 and the total stellar mass summed over all group members ranging from $\log M_{\rm star}/M_\odot \approx 10.2$–11.4. All of these galaxy groups have star-forming galaxies projected close to the QSO sightlines.

A comparison of the gas kinematics between Ne VIII and O VI shows that Ne VIII typically exhibits a line width that is

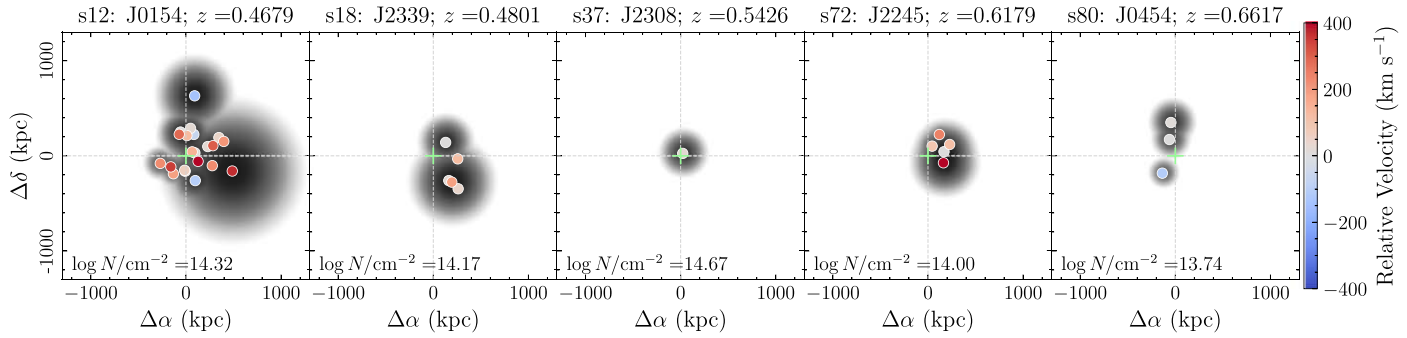

Figure 12. Summary of the galactic environments of newly detected Ne VIII systems in the CUBS-midz sample. The Ne VIII column densities are labeled in the lower-left corner of each panel, and the redshift at the top right. The QSO sightline is located at the center of each panel, marked by a green plus. The colors represent the velocity offsets, as shown in the color bar on the right, of individual galaxies relative to the redshift of the galaxy with the smallest $d_{\rm proj}/r_{200}$. To visualize the galaxy environment, we model each associated galaxy using a 2D Gaussian, with the FWHM representing r_{200} and amplitude representing the inferred halo mass. With the exception of one Ne VIII associated with a single star-forming disk galaxy at $z = 0.5426$ (middle panel), the remaining four absorbers are all found in an overdense galaxy environment.

either comparable or broader than O VI, indicating that at least some Ne VIII absorbers do not share the same origin as O VI. This may be due to blending in Ne VIII components if these components exhibit broader b values. It is worth noting that O VI in system s18 at $z = 0.4801$ is exceptionally strong, with a 2σ lower limit of $\log N/{\rm cm}^{-2} > 14.9$. The doublet features cannot be explained by either an interloper Lyα or Lyβ line because of a lack of corresponding higher-order Lyman series lines at shorter wavelengths. The aligned line centroid between O VI and Ne VIII but substantially narrower O VI lines suggest that local ionizing radiation or nonequilibrium processes may be crucial for explaining the exceptional strength of O VI.

Finally, the lack of O VI makes system s72 a special case, which is rare in all previous Ne VIII systems (e.g., Savage et al. 2005; Narayanan et al. 2011; Meiring et al. 2013; Burchett et al. 2019). In this system, we are able to place a 2σ upper limit of $\log N/{\rm cm}^{-2} < 13.9$ for the possible presence of O VI, while the Ne VIII lines are detected at a significance of $\approx 4\sigma$ and $\approx 2\sigma$ for the strong and weak members, leading to a total significance of $\approx 5\sigma$. Although individual components of low ions (e.g., H I and C III) are detected with a similar line centroid to the potential Ne VIII component, the dramatically different ionization potentials make it unlikely for these low ions to share the same ionization phase with Ne VIII. We include this system as a Ne VIII detection in all analyses, but it is still possible that the matched Ne VIII doublet may be due to contaminating absorption features at different redshifts.

5.2. Covering Fraction of Ne VIII

As a tracer of the warm-hot CGM, Ne VIII absorption has been detected in FUV spectra of background QSOs (e.g., Savage et al. 2005; Mulchaey & Chen 2009; Narayanan et al. 2011, 2012; Meiring et al. 2013; Qu & Bregman 2016), although the first Ne VIII search in a blind galaxy sample established without prior knowledge of existing features was carried out by the CASBaH survey (Burchett et al. 2019). A high covering fraction of $\kappa \approx 44 \pm 20\%$ was found at $d < 200$ kpc for a Ne VIII of $\log N/{\rm cm}^{-2} > 14.0$. Taken at face value, we would expect to detect $\sim$10 new strong Ne VIII absorbers with $\log N/{\rm cm}^{-2} > 14.0$ for 23 galaxies with $\log M_{\rm star}/M_\odot > 9$ and meaningful constraints on Ne VIII projected within 200 kpc from QSO sightlines in the CUBS-midz sample, but only five were found. Here, we examine possible factors that may have contributed to this discrepancy.

The CASBaH galaxies span a range in $M_{\rm star}$ from $\log M_{\rm star}/M_\odot \approx 9.0$–$11.3$ with a median of 10.1 and a standard deviation of 0.6 dex. The lowest-mass galaxies presented by the CASBaH are still more than an order of magnitude more massive than the low-mass galaxies in the CUBS-midz sample (see, e.g., Figure 2). Therefore, the first step toward a systematic comparison is to establish a comparable galaxy sample. To this end, we select all galaxies with $\log M_{\rm star}/M_\odot > 9.0$ in the CUBS-midz sample, which has a median of 10.3 and a standard deviation of 0.7 dex.

Given the challenge of robustly identifying a Ne VIII absorber in the presence of numerous interlopers, we also adopt a conservative column density threshold of $\log N_0/{\rm cm}^{-2} = 14.0$ for computing the covering fraction. To obtain accurate constraints for the gas covering fraction, particularly in the event of a small sample, it is critical to first establish a uniform sample of absorption spectra that offers a consistent sensitivity limit for detecting both strong and weak absorbers. While strong absorbers can be detected in both low- and high-S/N data, weak absorbers can only be detected in high-S/N spectra. Including low-S/N sightlines based on the presence of a strong absorber, instead of matching sensitivities, would lead to an overestimate of the gas covering fraction. For this reason, we estimate a limiting column density in continuum regions around all detections to identify and exclude those low-S/N sightlines even when a strong absorber is reported. This exercise leads to 57 and 26 galaxies/galaxy groups with sufficient sensitivities in the background QSO spectrum to detect Ne VIII absorbers of $\log N_{\rm NeVIII}/{\rm cm}^{-2} > 14$ in the CUBS and CASBaH surveys, respectively, projected within $3r_{200}$.

In Figure 13, covering fractions are shown as functions of both $d_{\rm proj}$ and $d_{\rm proj}/r_{200}$. We adopt all reported Ne VIII and their $\log N_{\rm NeVIII}/{\rm cm}^{-2}$ from Burchett et al. (2019) for the panel on r_{200}, but compute the covering fraction versus $d_{\rm proj}/r_{200}$ ourselves because these are not reported in Burchett et al. (2019). All covering fractions obtained from the CUBS and CASBaH samples are consistent with each other within 1σ at all radii, showing significant declines beyond 200 kpc or r_{200}. However, the CUBS sample prefers lower covering fractions than the CASBaH survey. Specifically, the CUBS sample exhibits a covering fraction of $18^{+9}_{-7}\%$ for Ne VIII absorbers with $\log N/{\rm cm}^{-2} > 14.0$, while the CASBaH sample prefers $44^{+22}_{-20}\%$ within 200 kpc. Within r_{200}, the CUBS and CASBaH samples show $36^{+18}_{-16}\%$ and $50 \pm 17\%$, respectively. Here, the

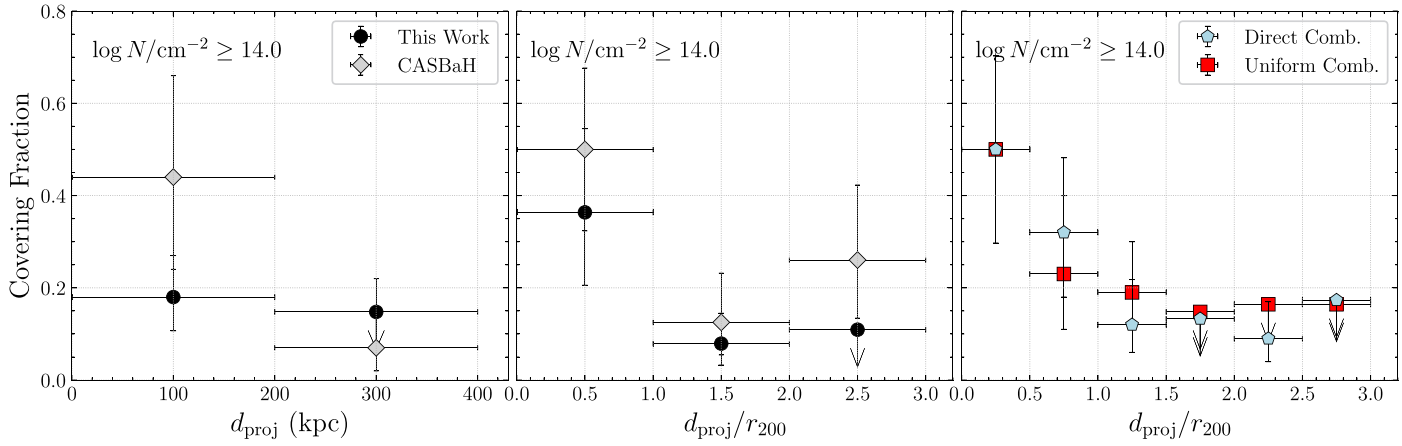

Figure 13. Covering fractions of Ne VIII absorption features with $\log N/\mathrm{cm}^{-2} \geqslant 14.0$ as functions $d_{\rm proj}$ (the left panel) and $d_{\rm proj}/r_{200}$ (middle and right panels). Here, we filter the stellar mass $\log M_{\rm star}/M_{\odot} > 9.0$ of galaxies in the CUBS program to match with the CASBaH sample (see the text for the details). In the left two panels, the CUBS sample (black circles) and the CASBaH sample (gray diamonds) are presented separately. Although the results from the two samples are consistent within the 1σ uncertainties, the covering fractions estimated using the CUBS sample are consistently lower than the CASBaH measurements. In the right panel, we show the covering fractions at $\log N/\mathrm{cm}^{-2} \geqslant 14.0$, combining both samples. We report two sets of combined covering fraction measurements. The first is calculated including all Ne VIII reported by the CASBaH team (light blue pentagons), while the second includes only absorbers that satisfy the same set of criteria as those from CUBS (red squares; see Section 4.1). This uniform, combined sample results in conservative measurements of the Ne VIII gas covering fraction, due to uncertainties in Ne VIII identifications.

covering fractions are higher than the values in Figure 6 because nondetections associated with low-mass galaxies are omitted from this comparison.

For an optimal statistical analysis, we combine the CUBS and CASBaH samples to assess how the gas covering fraction depends on $d_{\rm proj}/r_{200}$. This is presented in the right panel of Figure 13. We report two sets of measurements resulting from applying different treatments for the CASBaH sample. First, we calculate the combined covering fraction using all nine reported Ne VIII absorbers from Burchett et al. (2019). The results are shown as pentagons in the right panel of Figure 13. The measured covering fractions are summarized in Table 3 Second, we apply a uniform set of selection criteria of Ne VIII absorbers described in Section 4.1 for both samples and compute the gas covering fractions based on this uniform sample. This second set of measurements represents a conservative estimate of the gas covering fraction, due to the difficulties in robustly identifying Ne VIII in the presence of interlopers.

In summary, our analysis shows that the covering fraction Ne VIII declines with increasing distance out to $\approx 1.5 r_{200}$, and it may not be as high as previously thought around galaxies of $\log M_{\rm star}/M_{\odot} \approx 9.0$–$11.5$.

5.3. Total Mass of the Warm-hot CGM Probed by O VI and Ne VIII

To evaluate the mass budget of the warm-hot CGM, we first calculate the average column density within r_{200} using the best-fit column density profiles and covering fractions for galaxies in different subsamples presented in Section 4.2. Figure 14 shows the dependence of the area-weighted mean O VI column density with r_{200} on the stellar mass. The mean column density exhibits an increase of 0.8 dex from dwarfs to sub-L^* galaxies, followed by a decrease of 0.2 dex to massive star-forming galaxies. At $\log M_{\rm star}/M_{\odot} > 10.3$, massive quiescent galaxies on average exhibit a lower O VI column density in the CGM than star-forming galaxies (see also Zahedy et al. 2019).

We calculate the total enclosed O VI mass at $d_{\rm proj} < r_{200}$ and within the maximum radius, $d_{\rm proj} = 3r_{200}$, surveyed in this study (Figure 14). The total O VI mass increases from $d_{\rm proj} < r_{200}$ to $d_{\rm proj} < 3r_{200}$ by $\approx$0.2–0.3 dex for star-forming galaxies, while the increment is $\approx$0.6 dex for the massive quiescent galaxies. This is expected because of a flatter column density profile found in these massive quiescent halos. For the massive galaxy samples (i.e., star-forming and quiescent), the large error bars shown in Figure 14 also have significant contributions from the difference in halo sizes for different galaxies.

Table 3
Summary of the Observed Ne VIII Covering Fraction (%)

	$d_{\rm proj}/r_{200}$					
Sample	0.5	1.0	1.5	2.0	2.5	3.0
Direct	50 ± 20	32^{+17}_{-14}	12^{+9}_{-6}	<13	9^{+8}_{-5}	<17
Uniform	50 ± 20	23^{+17}_{-12}	19^{+11}_{-8}	<14	<17	<17

In Figure 14, we also include model predictions for the O VI mass, following a simple halo model. For each dark matter halo, we adopt a cosmic baryonic fraction of $f_{\rm b} = 0.156$ (Planck Collaboration et al. 2020), a fraction of the baryonic mass in the CGM, $f_{\rm CGM}$, and a fraction of oxygen in the O VI ionization state, $f_{\rm OVI}$. The expected total mass in O VI is then $M_{\rm OVI} = M_{\rm halo} f_{\rm b} f_{\rm CGM}/\mu \times A_{\rm O}({\rm O/H}) f_{\rm OVI}$, where $\mu = 1.4$ is the atom mass per hydrogen, $A_{\rm O} = 16$ is the atomic number of oxygen, and O/H is the number ratio between oxygen and hydrogen.

In the following discussion, we use $f_{\rm CGM} f_{\rm OVI} Z_{\rm O}/Z_{\rm O,\odot}$ as an integrated normalization of the model because these quantities are degenerate with one another. We adopt $Z_{\rm O}/Z_{\rm O,\odot}$ to represent the oxygen abundance relative to the solar value. We find that $f_{\rm CGM} f_{\rm OVI} Z_{\rm O}/Z_{\rm O,\odot} \approx 0.01$ is required to reproduce the observed O VI ion mass in sub-L^* galaxies, as shown in Figure 14, which displays the highest mean $N_{\rm OVI}$. A typical metallicity in the CGM is $\approx 0.3\, Z_{\odot}$, and the CGM mass fraction is predicted to be 0.1–0.5 in recent simulations (e.g., Wijers et al. 2020). Adopting a typical gas-phase metallicity and $f_{\rm CGM}$, we obtain an average ionization fraction of $\approx$0.05–0.3 for O VI,

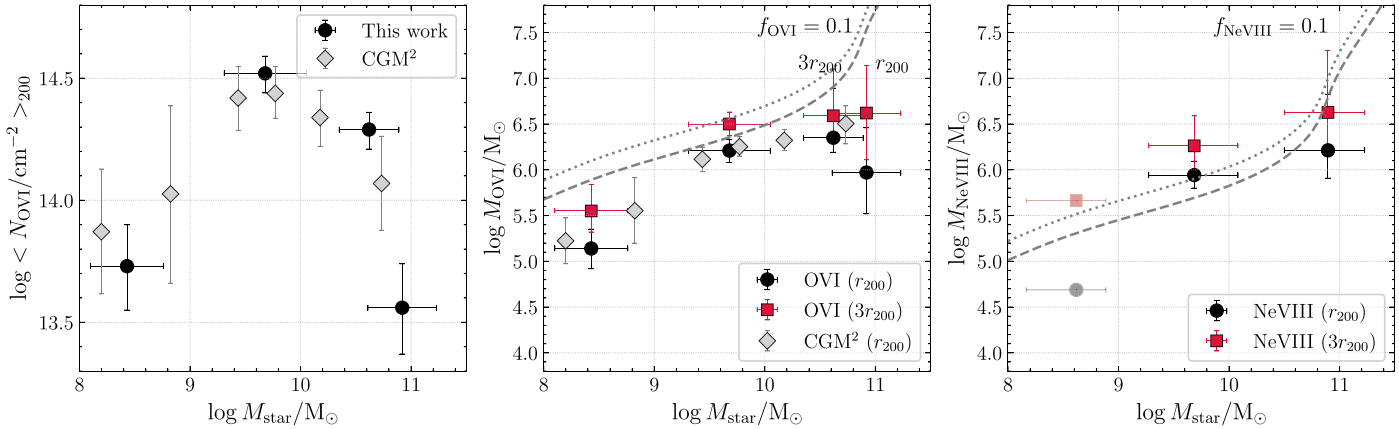

Figure 14. Mass content of the warm-hot CGM probed by O VI and Ne VIII vs. M_{star}. Left panel: dependence of mean N_{OVI} averaged within r_{200} on the stellar mass (black circles). The mean N_{OVI} peaks at $\log M_{star}/M_\odot \approx 10$. For comparison, we include the mean column density of star-forming galaxies adopted from (Tchernyshyov et al. 2022, gray diamonds). Middle panel: total O VI gas mass within r_{200} (black circles) or $3r_{200}$ (red squares). Extending to $\approx 3r_{200}$, the total O VI mass is a factor of $\approx$2–4 larger than the mass within r_{200} for all galaxies. As a comparison, we include the expected total O VI mass within r_{200} (the dashed line) and $3r_{200}$ (the dotted line) based on a model assuming a cosmic baryonic fraction, $f_b = 0.156$, and an anticipated fraction of baryonic mass in O VI, $f_{OVI} f_{CGM} Z_O/Z_{O,\odot} = 0.01$. Adopting typical f_{CGM} and $Z_O/Z_{O,\odot}$, we obtain $f_{OVI} \approx 0.1$ to reproduce the observed O VI content in the CGM of sub-L^* galaxies, suggesting that O VI-bearing gas is the dominant phase in these galaxies (see the text for the details). Right panel: Ne VIII mass, similar to the middle panel. The Ne VIII mass is calculated empirically, which may be driven by the highest column density absorbers at small d_{proj}/r_{200} (see the text for the details).

which is comparable with the peak ionization fraction of 0.2–0.4 in CIE or PIE models (e.g., Oppenheimer & Schaye 2013; S18). Therefore, we conclude that O VI-bearing gas is an important phase in these sub-L^* halos. We also plot the model-predicted mass out to $3r_{200}$, extrapolating an NFW (Navarro et al. 1996) halo profile with a concentration of 4 for star-forming galaxies. For sub-L^* galaxies, the predicted O VI is consistent with observations, indicating O VI is also abundant in the outskirts of these galaxy halos. On the other hand, the observed O VI mass in the CGM of dwarf galaxies or massive quiescent galaxies is significantly lower than the model prediction, suggesting that the typical ionization state in these halos is offset from O VI, assuming $f_{CGM} \approx 0.3$ (see also Zahedy et al. 2019; Zheng et al. 2024). However, the CGM mass fraction in dwarf galaxies may be as low as $\approx$0.1 (e.g., Schaller et al. 2015; Hafen et al. 2019), which also affects the O VI mass.

For Ne VIII, no best-fit model is available because of the small sample of detections. Therefore, the Ne VIII mass is calculated by summing over all available empirical constraints, including both measurements and upper limits. Specifically, we divide the radial profile into discrete bins and calculate a median Ne VIII column density in each bin. For nondetections, we estimate a median column density, $\langle N \rangle$ that satisfies $\mathrm{erf}(\langle N \rangle / N^{68}) = \frac{1}{2}\,\mathrm{erf}(N^{95}/N^{68})$, where erf() is the error function and N^{68} and N^{95} represent the 68% and 95% upper limits, respectively. The empirically determined Ne VIII masses are plotted in the right panel of Figure 14.

Similar to O VI, we also plot the simple model prediction of the Ne VIII mass, assuming $f_{CGM} f_{NeVIII} Z_{Ne}/Z_{Ne,\odot} \approx 0.01$. As a lithium-like ion, Ne VIII shares a similar ionization fraction as O VI, with a peak of $f_{NeVIII} \approx 0.2$ and 0.4 in CIE and PIE, respectively (e.g., Oppenheimer & Schaye 2013). The observed Ne VIII mass is higher than the model prediction for the sub-L^* sample. However, we note for both the sub-L^* and massive galaxy samples, the mass estimates are driven by a few high column density systems at the smallest d_{proj}/r_{200}, which contribute 30%–40% of the total Ne VIII mass. The total mass estimate is, therefore, subject to large stochastic uncertainties.

We note that a systematic uncertainty in the mass budget calculation may be induced by the halo model adopted for estimating r_{200}. Compared to the CGM^2 survey, for sub-L^* and massive star-forming galaxies, our mean O VI column densities are higher than the values reported in CGM^2 by 0.1–0.2 dex. This difference is mainly due to a different adopted SMHM relation for computing r_{200}. As stated in Section 2, we adopted the Kravtsov et al. (2018) relation that includes missing light correction in the total stellar mass of massive galaxies. This leads to a smaller inferred halo mass by $\approx$0.1–0.2 dex for a given M_{star} at $\log M_{star}/M_\odot \approx 9.5$–$10.5$, compared to the Behroozi et al. (2019) model. Using the Behroozi et al. (2019) model, we would infer a higher halo mass, and as a result, a larger r_{200}. A larger r_{200} would lower the mean column density within r_{200} by including more nondetections at larger projected distances.

5.4. Spatial Variation of the N_{NeVIII}/N_{OVI} Ratio

The origin of the warm-hot CGM may be explained by different scenarios, including the virialized ambient gas, the outflowing ejection from the galaxy disk, and cooling gas from the hotter phase (e.g., Oppenheimer et al. 2016; McQuinn & Werk 2018; S18; QB18; Wijers et al. 2024). The observed N_{NeVIII}/N_{OVI} ratio provides valuable insights into the ionization mechanisms of the warm-hot CGM and its origin. In particular, we consider two different model scenarios: photoionized gas versus radiative cooling gas in the hot halo (see S18 and QB18). These models predict distinct behaviors for N_{NeVIII}/N_{OVI} in different scenarios. However, the current sample is still too small to establish a consistent physical understanding of the ionization mechanism of these absorbers. Here, we compare the existing sample with model predictions to shed light on future observations.

S18 introduced two scenarios to generate O VI and Ne VIII in the CGM of star-forming L^* galaxies. These authors considered the possibility that the warm-hot CGM is photoionized in the low-density and low-pressure halo. This low-pressure scenario shows a clear increase in N_{NeVIII}/N_{OVI} with increasing

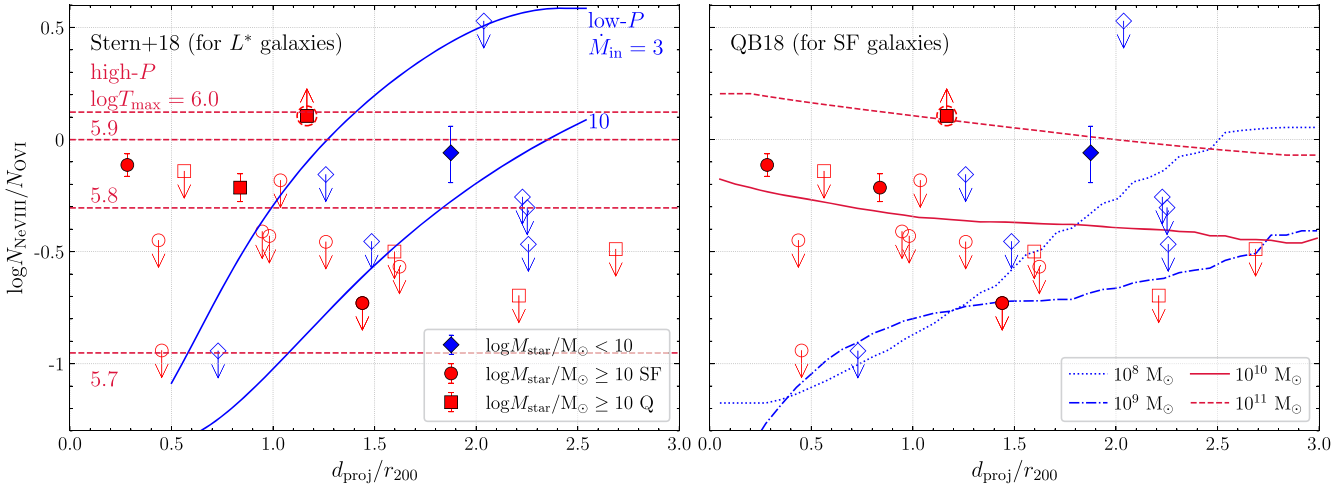

Figure 15. Comparison of dependence of $N_{\rm NeVIII}/N_{\rm OVI}$ on $d_{\rm proj}/r_{200}$ between data and models. Photoionization-dominated models predict increasing of $N_{\rm NeVIII}/N_{\rm OVI}$ at larger $d_{\rm proj}/r_{200}$ in (i.e., low-pressure models in the left panel, S18; and models for low-mass $\log M_{\rm star}/M_\odot \lesssim 9$ in the right panel, QB18). The warm-hot gas in cooling gas or virialized gas suggests roughly constant $N_{\rm NeVIII}/N_{\rm OVI}$ over different radii (i.e., high-pressure models in the left panel and models for massive $\log M_{\rm star}/M_\odot \gtrsim 10$ in the right panel). For observations, only absorption systems with at least O VI or Ne VIII features are included to ensure meaningful constraints. The small sample size limits the ability to distinguish between models. Open symbols represent upper limits in Ne VIII, while O VI is a detection. The filled red circle with a downward arrow denotes s18 at $z = 0.4801$, for which both Ne VIII and O VI are detected but the O VI is exceptionally strong and saturated. The full sample is divided into a low-mass star-forming sample with $\log M_{\rm star}/M_\odot \leqslant 10$ (blue diamonds), massive star-forming (red circles), and quiescent samples (red squares) with $\log M_{\rm star}/M_\odot > 10$.

projected distance because of a declining gas density (Figure 15). The predicted ion ratios from this low-pressure model presented in Figure 15 are for two different mass inflow rates, $\dot{M}_{\rm in} = 3$ and 10 $M_\odot\,{\rm yr}^{-1}$; see S18 for the details).

S18 also considered the possibility that the warm-hot gas arises in the high-pressure cooling flow from the hot phase (see also Stern et al. 2019, 2024). In this high-pressure scenario, the $N_{\rm NeVIII}/N_{\rm OVI}$ ratio only depends on the maximum temperature of the cooling flow, which shows no radial dependence.

QB18 developed a hybrid model for galaxies in different mass ranges. For a gaseous halo around galaxies of $M_{\rm star} \approx 10^8$–$10^{11}\,M_\odot$, these authors attributed the warm-hot gas to cooling gas from the hot halos and accounted for photoionization due to the UVB by adopting the ionization fractions from Oppenheimer & Schaye (2013). In low-mass galaxies of $M_{\rm star} \approx 10^8$–$10^9\,M_\odot$, the virial temperature is too low to form O VI and Ne VIII through collisional ionization. Therefore, the measured warm-hot CGM is photoionized, which shows increasing $N_{\rm NeVIII}/N_{\rm OVI}$ with radius. For massive galaxies of $M_{\rm star} \gtrsim 10^{10}\,M_\odot$, the QB18 model predicts relatively constant $N_{\rm NeVIII}/N_{\rm OVI}$ with radius because the warm-hot gas is mainly collisionally ionized at the peak temperature.

Figure 15 shows comparisons between predicted and observed $N_{\rm NeVIII}/N_{\rm OVI}$ ratios at different projected distances. The observed $N_{\rm NeVIII}/N_{\rm OVI}$ ratios are presented for absorbers with at least one ion detected (i.e., O VI or Ne VIII). In total, 23 individual systems have meaningful constraints on $N_{\rm NeVIII}/N_{\rm OVI}$, including all five newly discovered Ne VIII absorbers (see Section 5.1).

The galaxy sample is divided into three subsamples according to $M_{\rm star}$ and SFR. For low-mass galaxies of $\log M_{\rm star}/M_\odot < 10$, the only measured $N_{\rm NeVIII}/N_{\rm OVI}$ is at $\approx 2r_{200}$. This is consistent with the photoionization scenario, although no trend can be derived with only one detection in this mass range. For massive galaxies of $\log M_{\rm star}/M_\odot \geqslant 10$, we further group them into star-forming and quiescent galaxy subsamples with an SFR threshold of $0.2\,M_\odot{\rm yr}^{-1}$. These two subsamples exhibit similar $N_{\rm NeVIII}/N_{\rm OVI}$ ratios. For massive star-forming galaxies, two systems with both Ne VIII and O VI detected show $N_{\rm NeVIII}/N_{\rm OVI}$ of ≈0.6–1, suggesting a temperature of $\log T/{\rm K} \approx 5.8$ in either the collisional ionization scenarios (e.g., Savage et al. 2005; Meiring et al. 2013; McQuinn & Werk 2018).

We note two special cases. For s72 with an $N_{\rm NeVIII}/N_{\rm OVI}$ ratio of $\gtrsim$1.2, the associated galaxy at the smallest $d_{\rm proj}/r_{200}$ is the most massive with $\log M_{\rm star}/M_\odot \approx 10.6$ among all five detected Ne VIII absorbers. This is indeed expected from the cooling flow model, in which massive galaxies should produce the highest $N_{\rm NeVIII}/N_{\rm OVI}$ ratio (QB18). For s18 with an $N_{\rm NeVIII}/N_{\rm OVI}$ ratio of $\lesssim$0.2, the observed O VI is exceptionally strong and narrow, suggesting a photoionized origin or a nonequilibrium condition. It is, therefore, likely that this system is significantly affected by local radiation due to nearby galaxies (see examples in Zahedy et al. 2021; CUBS VI).

Given the distinct predictions for $N_{\rm NeVIII}/N_{\rm OVI}$ from different model scenarios, our sample at the moment is still too small to establish a consistent physical understanding of the origin of these absorbers. In particular, existing data do not provide a sufficiently large dynamic range in the $N_{\rm NeVIII}/N_{\rm OVI}$ ratio to discriminate different models. Improving the detection limit of Ne VIII with high-S/N ratio spectra is necessary to strengthen these model comparisons.

6. Summary

In this work, we establish the CUBS-midz sample of $0.4 \lesssim z \lesssim 0.7$ galaxies with small projected distances to the 15 CUBS background QSOs (Figure 2), aiming to study the warm-hot CGM probed by the O VI and Ne VIII doublets. The new sample contains 50 individual galaxies and 53 galaxy groups with two to 21 member galaxies. In this sample, 30 O VI and five Ne VIII absorbers are detected. Combining the CUBS-midz sample with literature samples, we investigate the radial dependence of line-of-sight absorption properties

(e.g., the column density and velocity dispersion) on galaxy stellar masses and SFRs. Our major results are summarized below.

1. Detected O VI and Ne VIII absorption features exhibit column densities of $\log N/\mathrm{cm}^{-2} \approx 13.5$–$15.0$, while the limiting column densities are $\log N/\mathrm{cm}^{-2} \approx 13.7$ and 14.0, respectively, for a large fraction of nondetections. We calculate the velocity dispersion of detected O VI and Ne VIII features, spanning from $\approx$5–120 km s^{-1} (Figure 3). In particular, we consider features with $\sigma_v \gtrsim 40$ km s^{-1} as broad features, tracing the kinematics in the halo instead of the internal velocity dispersion in individual clouds.
2. We examine the correlations between the O VI and Ne VIII properties and different nearby galaxies with the smallest d_{proj}, smallest $d_{\mathrm{proj}}/r_{200}$, and highest M_{star}, using the 53 sightlines probing the overdense galaxy environments with multiple nearby galaxies (Figures 4 and 5). The observed O VI column density and kinematics are most correlated with the galaxy with the smallest $d_{\mathrm{proj}}/r_{200}$, which is therefore taken as the host galaxy of absorption features in group environments.
3. The detected O VI and Ne VIII absorption features exhibit bulk velocities within $\approx$200 km s^{-1} relative to the associated galaxies (Figure 5). Normalized by the escape velocity, the bulk velocity distribution can be modeled by a Gaussian function with a standard deviation of $\sigma \approx 0.40$.
4. For both O VI and Ne VIII, particularly high column density and broad absorption features are detected around galaxies with $M_{\mathrm{star}}/M_{\odot} \approx 10$ (Figures 7 and 8).
5. For O VI, we divide the CUBS-midz sample into four subsamples based on M_{star} and SFR: the dwarf, sub-L^*, massive star-forming, and massive quiescent galaxy samples. Combined with literature samples, the sub-L^* and massive star-forming galaxy samples show substantial radial declines of column density with a power-law slope of $\approx$0.8, while the massive quiescent galaxy sample exhibits flatter radial profiles (Figure 9).
6. The covering fraction of O VI is high ($\approx$90%–100%) for sub-L^* and massive star-forming galaxies within the virial radius, and exhibits a sharp decline at 1–2r_{200}. The massive quiescent galaxies exhibit a roughly constant covering fraction of $\approx$30% out to 3r_{200} (Figure 9). The joint observations of flat covering fraction and column density profiles suggest less concentrated O VI-bearing gas in the CGM of quiescent galaxies.
7. For Ne VIII, we divide the sample into three subsamples based only on M_{star}, considering the small sample of Ne VIII detections. Within r_{200}, the sub-L^* galaxy sample exhibits a higher covering fraction of high N_{NeVIII} systems with $\log N_{\mathrm{NeVIII}}/\mathrm{cm}^{-2} \geqslant 14.0$ (Figure 10).
8. We compare the covering fraction of Ne VIII with the CASBaH sample for galaxies with $\log M_{\mathrm{star}}/M_{\odot} \approx 9$–$11.5$, showing that the CUBS sample exhibits relatively lower covering fractions over all radii for a limiting $\log N_{\mathrm{NeVIII}}/\mathrm{cm}^{-2} = 14.0$ (Figure 13 and Table 3).
9. The warm-hot CGM probed by O VI and Ne VIII dominates the CGM of sub-L^* galaxies, exhibiting the highest area-weighted mean column density within r_{200} (Figure 14). Adopting a typical metallicity and CGM mass fraction, we show that ionization fractions of O VI and Ne VIII are comparable with the peak ionization fraction in CIE or PIE models, suggesting the warm-hot CGM probed by O VI and Ne VIII is the dominant phase in halos of sub-L^* galaxies.

Acknowledgments

We thank the anonymous referee for a careful review and valuable suggestions that significantly improved our work. The authors thank Jonathan Stern for sharing their models of $N_{\mathrm{NeVIII}}/N_{\mathrm{OVI}}$ ratio in L^* galaxies. Z.Q. acknowledges partial support from HST-GO-15163.001A, NSF AST-1715692 grants, and NASA ADAP grant 80NSSC22K0481. H.W.C. and M.C.C. acknowledge partial support from HST-GO-15163.001A and NSF AST-1715692 grants. S.D.J. acknowledges partial support from HST-GO-15280.009A. G.C.R. acknowledges partial support from HST-GO-15163.015A. F.S.Z. acknowledges the support of a Carnegie Fellowship from the Observatories of the Carnegie Institution for Science. D.D. acknowledges the support of the John A. Lyons Fellowship from MIT's Office of Graduate Education. E.B. acknowledges partial support from NASA under award No. 80GSFC21M0002. S.C. gratefully acknowledges support from the European Research Council (ERC) under the European Unions Horizon 2020 research and innovation program grant agreement No 864361. CAFG was supported by NSF through grants AST-2108230, AST-2307327, and CAREER award AST-1652522; by NASA through grants 17-ATP17-0067 and 21-ATP21-0036; by STScI through grants HST-GO-16730.016-A and JWSTAR-03252.001-A; and by CXO through grant TM2-23005X. J.I.L. is supported by the Eric and Wendy Schmidt AI in Science Postdoctoral Fellowship, a Schmidt Futures program. This work is based on observations made with ESO Telescopes at the Paranal Observatory under program ID 0104.A-0147(A), observations made with the 6.5 m Magellan Telescopes located at Las Campanas Observatory, and spectroscopic data gathered under the HST-GO-15163.01A program using the NASA/ESA Hubble Space Telescope operated by the Space Telescope Science Institute and the Association of Universities for Research in Astronomy, Inc., under NASA contract NAS 5-26555. This research has made use of the services of the ESO Science Archive Facility and the Astrophysics Data Service (ADS).[16] The analysis in this work was greatly facilitated by the following `Python` packages: `NumPy` (Harris et al. 2020), `SciPy` (Virtanen et al. 2020), `Astropy` (Astropy Collaboration et al. 2013; Price-Whelan et al. 2018), `Matplotlib` (Hunter 2007), and `emcee` (Foreman-Mackey et al. 2013).

Appendix A
Connecting Ne VIII Absorbers to Galaxies in the Presence of Neighbors

In Figure A1, we show the N_{NeVIII} dependence on d_{proj} and $d_{\mathrm{proj}}/r_{200,}$ adopting the three galaxy associations described in Section 3.1. Unlike O VI, the small number of Ne VIII detections leads to no clear trend.

[16] https://ui.adsabs.harvard.edu

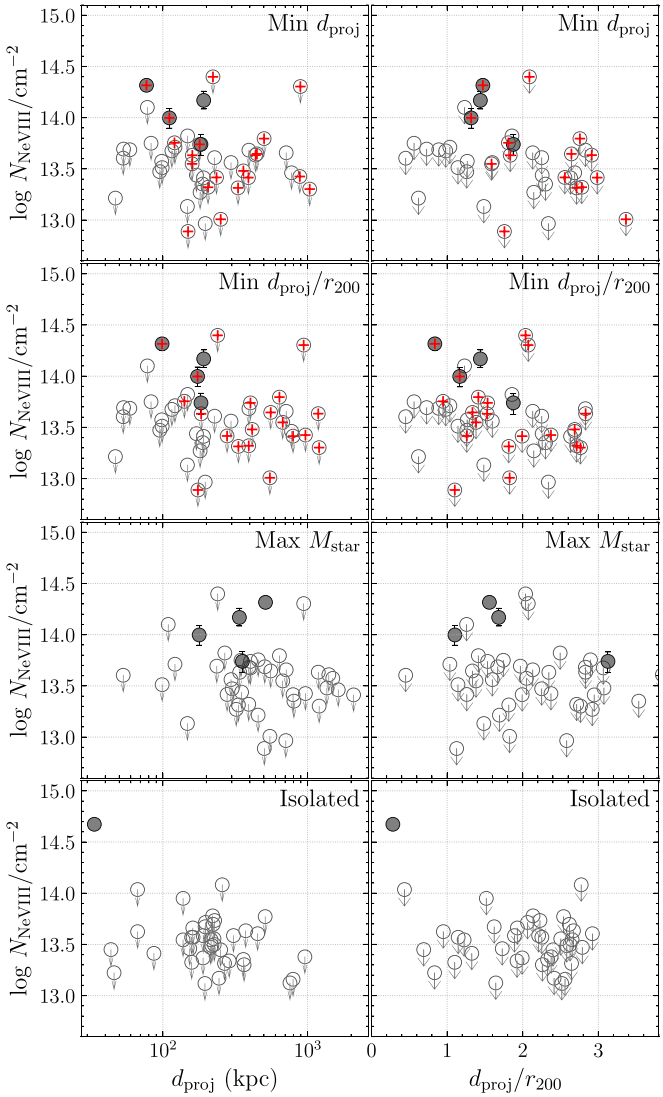

Figure A1. Similar to Figure 4 but for the observed constraints on the Ne VIII column densities. Unlike O VI, few galaxies/galaxy groups display detectable Ne VIII absorption. No clear trend can be established in any panels.

Appendix B
Summary of Galaxy and Absorber Properties

The galaxy and absorber properties used in this study are summarized in Table B1.

Table B1
Summary of Galaxy and Absorber Properties

QSO	ID	$N_{\rm gal}$	$z_{\rm gal}$	$\log M_{\rm star}$ $/M_\odot$	SFR $M_\odot\ {\rm yr}^{-1}$	$d_{\rm proj}$ kpc	$d_{\rm proj}$ $/r_{200}$	$\log \psi/G$ $/(M_\odot/{\rm kpc})$	$\log N_{\rm OVI}$ $/{\rm cm}^{-2}$	$\sigma_{\rm OVI}$ km s^{-1}	$v_{\rm OVI}$ km s^{-1}	$\log N_{\rm NeVIII}$ $/{\rm cm}^{-2}$	$\sigma_{\rm NeVIII}$ km s^{-1}	$v_{\rm NeVIII}$ km s^{-1}
J0454	s1	4	0.4315	10.4 ± 0.1	<0.1	82	0.56	10.1	$13.89^{+0.03}_{-0.03}$	$16.4^{+2.1}_{-1.9}$	$-72.4^{+2.1}_{-1.9}$	<13.8	⋯	⋯
J0357	s2	1	0.4358	10.5 ± 0.1	0.6 ± 0.2	66	0.44	10.0	$14.49^{+0.02}_{-0.02}$	$80.8^{+6.3}_{-6.9}$	$-63.6^{+5.8}_{-6.3}$	<14.0	⋯	⋯
J0154	s3	1	0.4393	10.5 ± 0.1	0.8 ± 0.4	452	2.92	9.2	<12.8	⋯	⋯	<13.6	⋯	⋯
J0028	s4	1	0.4420	9.2 ± 0.1	0.3 ± 0.2	197	2.06	8.9	<12.9	⋯	⋯	<13.7	⋯	⋯
J0357	s5	1	0.4490	8.2 ± 0.1	0.2 ± 0.1	66	0.95	9.0	⋯	⋯	⋯	<13.6	⋯	⋯
J2135	s6	3	0.4499	9.6 ± 0.1	2.1 ± 0.3	142	1.33	9.9	$14.35^{+0.02}_{-0.02}$	$18.0^{+1.2}_{-1.0}$	$6.4^{+1.0}_{-1.0}$	⋯	⋯	⋯
J0119	s7	5	0.4519	10.5 ± 0.1	1.3 ± 0.3	140	0.95	9.9	$14.16^{+0.02}_{-0.03}$	$22.1^{+2.4}_{-1.9}$	$-25.0^{+1.6}_{-1.6}$	<13.8	⋯	⋯
J0154	s8	1	0.4551	7.9 ± 0.4	0.2 ± 0.1	43	0.69	9.0	<13.0	⋯	⋯	<13.4	⋯	⋯
J0119	s9	1	0.4668	8.6 ± 0.2	0.3 ± 0.2	215	2.65	8.7	<13.0	⋯	⋯	<13.5	⋯	⋯
J0111	s10	1	0.4669	8.3 ± 0.3	0.1 ± 0.1	91	1.28	8.9	$13.86^{+0.05}_{-0.06}$	$30.8^{+4.8}_{-4.3}$	$58.5^{+1.1}_{-2.1}$	⋯	⋯	⋯
J0114	s11	3	0.4671	$9.9^{+0.1}_{-0.2}$	1.4 ± 0.3	239	2.04	9.4	$13.87^{+0.08}_{-0.11}$	$33.0^{+12.2}_{-7.7}$	$-13.3^{+6.2}_{-3.2}$	<14.4	⋯	⋯
J0154	s12	21	0.4679	10.0 ± 0.1	0.3 ± 0.1	98	0.84	10.5	$14.53^{+0.02}_{-0.02}$	$44.9^{+1.2}_{-1.3}$	$99.6^{+2.0}_{-1.6}$	$14.32^{+0.06}_{-0.06}$	$46.9^{+7.5}_{-7.4}$	$127.9^{+0.2}_{-1.1}$
J0110	s13	2	0.4725	10.0 ± 0.1	0.5 ± 0.2	53	0.45	9.8	$14.55^{+0.02}_{-0.02}$	$95.1^{+1.6}_{-1.8}$	$75.2^{+3.1}_{-3.1}$	<13.6	⋯	⋯
J0119	s14	1	0.4727	9.6 ± 0.1	0.9 ± 0.2	250	2.40	8.9	<13.2	⋯	⋯	<13.4	⋯	⋯
J0028	s15	4	0.4743	8.4 ± 0.2	0.2 ± 0.1	95	1.26	9.5	$13.63^{+0.07}_{-0.07}$	$21.8^{+5.4}_{-4.5}$	$-15.5^{+4.8}_{-5.0}$	<13.5	⋯	⋯
J2308	s16	1	0.4781	10.0 ± 0.1	1.0 ± 0.3	195	1.62	9.2	$14.24^{+0.03}_{-0.03}$	$19.0^{+2.2}_{-2.2}$	$-23.5^{+2.2}_{-2.3}$	<13.7	⋯	⋯
J0357	s17	6	0.4786	8.4 ± 0.1	0.1 ± 0.1	47	0.62	10.3	<12.9	⋯	⋯	<13.2	⋯	⋯
J2339	s18	5	0.4801	10.3 ± 0.1	0.4 ± 0.2	191	1.44	9.9	>14.9	$6.3^{+2.1}_{-1.1}$	$249.6^{+1.1}_{-1.1}$	$14.17^{+0.09}_{-0.08}$	$32.0^{+14.8}_{-9.1}$	$244.5^{+5.5}_{-8.9}$
J0154	s19	1	0.4813	11.3 ± 0.1	<0.1	756	1.64	10.4	<13.2	⋯	⋯	<13.1	⋯	⋯
J2245	s20	1	0.4894	9.8 ± 0.1	0.1 ± 0.1	137	1.22	9.3	<13.5	⋯	⋯	<13.5	⋯	⋯
J0333	s21	1	0.5010	10.6 ± 0.1	0.4 ± 0.2	360	2.33	9.3	<12.7	⋯	⋯	<13.4	⋯	⋯
J0154	s22	2	0.5072	8.4 ± 0.4	0.1 ± 0.1	170	2.26	8.9	$13.91^{+0.04}_{-0.04}$	$19.1^{+3.1}_{-2.7}$	$39.0^{+2.9}_{-2.5}$	<13.4	⋯	⋯
J2135	s23	1	0.5083	$8.7^{+0.2}_{-0.3}$	0.2 ± 0.1	65	0.81	9.2	$13.90^{+0.05}_{-0.05}$	$33.2^{+6.6}_{-6.6}$	$-2.0^{+5.4}_{-5.0}$	⋯	⋯	⋯
J0111	s24	1	0.5140	8.7 ± 0.2	0.3 ± 0.2	238	2.94	8.6	<12.7	⋯	⋯	⋯	⋯	⋯
J0028	s25	3	0.5198	10.6 ± 0.1	5.3 ± 0.8	414	2.69	10.2	<12.8	⋯	⋯	<13.5	⋯	⋯
J0248	s26	1	0.5205	9.1 ± 0.1	<0.1	137	1.52	9.0	<13.2	⋯	⋯	<13.9	⋯	⋯
J0420	s27	7	0.5247	11.3 ± 0.1	<0.2	1203	2.76	10.2	<13.3	⋯	⋯	<13.3	⋯	⋯
J0248	s28	3	0.5265	11.3 ± 0.1	<0.1	940	2.07	10.3	<13.2	⋯	⋯	<14.3	⋯	⋯
J2339	s29	1	0.5277	8.8 ± 0.1	0.4 ± 0.2	218	2.58	8.7	<13.6	⋯	⋯	<13.5	⋯	⋯
J0357	s30	1	0.5306	9.5 ± 0.1	1.1 ± 0.3	244	2.41	8.9	<13.3	⋯	⋯	<13.2	⋯	⋯
J2245	s31	9	0.5338	8.1 ± 0.4	0.1 ± 0.1	59	0.89	10.3	<13.0	⋯	⋯	<13.7	⋯	⋯
J2308	s32	1	0.5364	9.6 ± 0.1	2.2 ± 0.3	228	2.23	9.0	$13.99^{+0.06}_{-0.05}$	$10.5^{+4.0}_{-2.9}$	$-31.9^{+2.0}_{-1.9}$	<13.7	⋯	⋯
J0111	s33	1	0.5367	9.4 ± 0.1	0.6 ± 0.2	222	2.31	8.9	<13.2	⋯	⋯	⋯	⋯	⋯
J0110	s34	10	0.5406	11.2 ± 0.1	0.6 ± 0.3	364	0.88	10.7	$13.80^{+0.06}_{-0.08}$	$14.8^{+3.9}_{-3.6}$	$138.4^{+3.1}_{-3.2}$	⋯	⋯	⋯
J0333	s35	4	0.5410	8.8 ± 0.2	0.1 ± 0.1	196	2.34	9.9	<13.1	⋯	⋯	<13.0	⋯	⋯
J0028	s36	1	0.5421	10.6 ± 0.1	0.2 ± 0.1	364	2.26	9.4	<13.6	⋯	⋯	<13.3	⋯	⋯
J2308	s37	1	0.5426	10.0 ± 0.1	1.9 ± 0.4	33	0.28	10.0	$14.79^{+0.02}_{-0.02}$	$67.7^{+2.4}_{-2.5}$	$-10.7^{+2.8}_{-3.2}$	$14.67^{+0.05}_{-0.05}$	$69.4^{+5.7}_{-6.1}$	$-31.5^{+8.7}_{-7.9}$
J0248	s38	1	0.5451	9.2 ± 0.2	0.5 ± 0.1	257	2.77	8.8	<13.3	⋯	⋯	<14.1	⋯	⋯
J0110	s39	1	0.5462	11.0 ± 0.1	<0.1	794	2.56	9.9	<13.3	⋯	⋯	<13.2	⋯	⋯
J2135	s40	1	0.5465	9.7 ± 0.1	0.8 ± 0.2	176	1.67	9.1	<13.1	⋯	⋯	⋯	⋯	⋯
J0154	s41	18	0.5491	10.6 ± 0.1	0.3 ± 0.1	174	1.10	10.9	<13.2	⋯	⋯	<12.9	⋯	⋯
J0357	s42	5	0.5497	8.7 ± 0.2	0.3 ± 0.1	148	1.86	9.5	<13.3	⋯	⋯	<13.8	⋯	⋯
J0420	s43	5	0.5533	11.0 ± 0.1	0.3 ± 0.2	403	1.54	10.0	<13.4	⋯	⋯	<13.7	⋯	⋯
J0119	s44	1	0.5534	9.5 ± 0.1	8.6 ± 1.3	190	1.89	9.0	<13.5	⋯	⋯	<13.6	⋯	⋯
J0357	s45	2	0.5561	8.9 ± 0.1	1.4 ± 0.2	98	1.14	9.2	<13.5	⋯	⋯	<13.5	⋯	⋯

Table B1
(Continued)

QSO	ID	$N_{\rm gal}$	$z_{\rm gal}$	$\log M_{\rm star}$ $/M_\odot$	SFR $M_\odot\ {\rm yr}^{-1}$	$d_{\rm proj}$ kpc	$d_{\rm proj}$ $/r_{200}$	$\log \psi/G$ $/(M_\odot/{\rm kpc})$	$\log N_{\rm OVI}$ $/{\rm cm}^{-2}$	$\sigma_{\rm OVI}$ km s^{-1}	$v_{\rm OVI}$ km s^{-1}	$\log N_{\rm NeVIII}$ $/{\rm cm}^{-2}$	$\sigma_{\rm NeVIII}$ km s^{-1}	$v_{\rm NeVIII}$ km s^{-1}
J0420	s46	7	0.5600	11.2 ± 0.1	<0.1	794	1.99	10.4	<13.2	⋯	⋯	<13.4	⋯	⋯
J0111	s47	1	0.5630	9.2 ± 0.1	⋯	159	1.72	9.0	<13.1	⋯	⋯	⋯	⋯	⋯
J0454	s48	1	0.5681	8.8 ± 0.2	⋯	161	1.93	8.9	<13.5	⋯	⋯	<13.7	⋯	⋯
J2135	s49	2	0.5717	8.6 ± 0.1	⋯	92	1.19	9.2	$14.18^{+0.04}_{-0.04}$	$17.4^{+2.3}_{-2.0}$	$-51.0^{+2.1}_{-2.2}$	⋯	⋯	⋯
J2339	s50	4	0.5728	8.4 ± 0.1	⋯	53	0.73	9.6	$14.64^{+0.04}_{-0.03}$	$36.1^{+4.8}_{-2.9}$	$-6.5^{+2.9}_{-3.5}$	<13.7	⋯	⋯
J0111	s51	8	0.5766	10.6 ± 0.1	<0.1	41	0.26	10.5	<13.5	⋯	⋯	⋯	⋯	⋯
J2245	s52	1	0.5785	10.9 ± 0.1	<0.1	509	2.54	9.5	<13.6	⋯	⋯	<13.8	⋯	⋯
J0454	s53	2	0.5811	11.3 ± 0.1	<0.5	639	1.41	10.5	<13.4	⋯	⋯	<13.8	⋯	⋯
J0119	s54	1	0.5812	$8.9^{+0.3}_{-0.4}$	0.1 ± 0.1	222	2.62	8.8	<13.3	⋯	⋯	<13.7	⋯	⋯
J2339	s55	1	0.5816	9.1 ± 0.2	0.5 ± 0.2	225	2.50	8.8	<13.3	⋯	⋯	<13.6	⋯	⋯
J0357	s56	4	0.5835	10.9 ± 0.1	1.8 ± 0.6	277	1.26	10.0	$13.87^{+0.06}_{-0.06}$	$26.0^{+5.0}_{-4.1}$	$79.9^{+4.7}_{-4.4}$	<13.4	⋯	⋯
J0420	s57	2	0.5838	9.0 ± 0.1	0.2 ± 0.1	79	0.90	9.7	$14.45^{+0.03}_{-0.03}$	$63.4^{+5.2}_{-4.6}$	$-17.1^{+5.6}_{-5.1}$	⋯	⋯	⋯
J2245	s58	2	0.5865	10.1 ± 0.1	0.5 ± 0.3	115	0.98	9.6	$14.11^{+0.05}_{-0.06}$	$49.3^{+4.3}_{-4.0}$	$28.6^{+8.0}_{-7.5}$	<13.7	⋯	⋯
J0333	s59	2	0.5872	10.8 ± 0.1	1.1 ± 0.4	332	1.82	9.7	<13.3	⋯	⋯	<13.3	⋯	⋯
J0114	s60	1	0.5887	$10.5^{+0.1}_{-0.2}$	1.1 ± 0.4	374	2.67	9.2	<13.5	⋯	⋯	<13.6	⋯	⋯
J0154	s61	4	0.5890	11.2 ± 0.1	<0.5	967	2.37	10.2	<13.7	⋯	⋯	<13.4	⋯	⋯
J0028	s62	1	0.5960	10.6 ± 0.1	0.1 ± 0.1	287	1.92	9.4	<13.6	⋯	⋯	<13.3	⋯	⋯
J0454	s63	1	0.6011	10.5 ± 0.1	<0.1	161	1.15	9.6	<13.2	⋯	⋯	<13.6	⋯	⋯
J0119	s64	9	0.6026	11.0 ± 0.1	<0.1	549	1.83	10.4	<13.2	⋯	⋯	<13.0	⋯	⋯
J0357	s65	1	0.6076	9.7 ± 0.2	<0.1	220	2.14	9.0	<13.4	⋯	⋯	<13.8	⋯	⋯
J0119	s66	10	0.6082	11.0 ± 0.1	<0.1	775	2.69	10.8	$13.95^{+0.07}_{-0.08}$	$25.7^{+6.0}_{-5.3}$	$98.4^{+5.7}_{-5.5}$	<13.5	⋯	⋯
J0110	s67	1	0.6097	9.6 ± 0.1	1.6 ± 0.4	266	2.65	8.9	<13.0	⋯	⋯	<13.3	⋯	⋯
J0028	s68	1	0.6134	11.2 ± 0.1	0.3 ± 0.2	959	2.38	10.2	<13.1	⋯	⋯	<13.4	⋯	⋯
J0154	s69	1	0.6141	10.5 ± 0.1	<0.1	158	1.10	9.6	<13.5	⋯	⋯	<13.3	⋯	⋯
J0454	s70	1	0.6150	9.0 ± 0.2	0.5 ± 0.2	226	2.63	8.8	<13.4	⋯	⋯	<13.5	⋯	⋯
J2308	s71	4	0.6161	11.1 ± 0.1	0.7 ± 0.4	712	2.13	10.1	<13.7	⋯	⋯	<13.7	⋯	⋯
J2245	s72	5	0.6179	10.6 ± 0.1	<0.1	173	1.17	10.1	<13.9	⋯	⋯	$14.00^{+0.09}_{-0.10}$	$26.3^{+10.2}_{-7.9}$	$63.1^{+6.6}_{-6.5}$
J2135	s73	13	0.6221	11.0 ± 0.1	0.7 ± 0.2	128	0.46	10.9	$14.84^{+0.32}_{-0.12}$	$24.6^{+10.4}_{-10.4}$	$-28.3^{+4.0}_{-2.5}$	⋯	⋯	⋯
J0357	s74	1	0.6258	9.1 ± 0.1	1.9 ± 0.2	153	1.73	9.0	<13.6	⋯	⋯	<13.5	⋯	⋯
J0111	s75	2	0.6300	11.0 ± 0.1	<0.1	501	1.93	10.0	<13.1	⋯	⋯	⋯	⋯	⋯
J2308	s76	1	0.6352	$8.6^{+0.3}_{-0.5}$	0.1 ± 0.1	214	2.79	8.7	<13.3	⋯	⋯	<13.5	⋯	⋯
J2245	s77	5	0.6386	10.2 ± 0.1	4.9 ± 0.5	184	1.53	9.9	<13.4	⋯	⋯	<13.6	⋯	⋯
J0111	s78	4	0.6483	10.9 ± 0.1	<0.1	59	0.29	10.6	<13.3	⋯	⋯	⋯	⋯	⋯
J2245	s79	2	0.6610	11.2 ± 0.1	<0.1	556	1.34	10.5	<13.6	⋯	⋯	<13.6	⋯	⋯
J0454	s80	3	0.6617	9.5 ± 0.1	2.4 ± 0.4	183	1.88	9.4	$13.80^{+0.08}_{-0.07}$	$25.0^{+6.0}_{-5.1}$	$-151.0^{+5.4}_{-5.7}$	$13.74^{+0.09}_{-0.11}$	<32.2	$-144.9^{+5.4}_{-6.5}$
J0420	s81	2	0.6641	10.1 ± 0.1	1.0 ± 0.2	121	1.04	9.6	$13.89^{+0.10}_{-0.11}$	$25.0^{+24.7}_{-8.1}$	$2.2^{+4.6}_{-6.4}$	<13.7	⋯	⋯
J2308	s82	2	0.6643	8.1 ± 0.3	0.1 ± 0.1	78	1.23	9.3	<13.2	⋯	⋯	<14.1	⋯	⋯
J0248	s83	1	0.6645	7.7 ± 0.1	0.3 ± 0.2	46	0.83	8.9	<13.1	⋯	⋯	<13.2	⋯	⋯
J0114	s84	2	0.6652	10.5 ± 0.2	0.3 ± 0.2	393	2.83	9.3	<14.0	⋯	⋯	<13.7	⋯	⋯
J2135	s85	1	0.6718	9.8 ± 0.1	0.5 ± 0.2	313	2.96	9.0	<13.1	⋯	⋯	⋯	⋯	⋯
J2339	s86	2	0.6724	9.0 ± 0.1	1.7 ± 0.3	180	2.15	9.3	<13.9	⋯	⋯	<13.3	⋯	⋯
J2135	s87	1	0.6758	7.8 ± 0.3	0.1 ± 0.1	33	0.59	9.1	$13.70^{+0.10}_{-0.13}$	$27.1^{+14.2}_{-10.9}$	$0.3^{+7.7}_{-9.0}$	⋯	⋯	⋯
J2339	s88	1	0.6779	8.2 ± 0.2	0.3 ± 0.2	86	1.33	8.9	<13.4	⋯	⋯	<13.4	⋯	⋯
J0357	s89	3	0.6802	8.4 ± 0.5	0.1 ± 0.1	191	2.63	10.7	<13.1	⋯	⋯	<13.4	⋯	⋯
J0333	s90	1	0.6802	$8.3^{+0.3}_{-0.4}$	0.1 ± 0.1	158	2.25	8.7	<13.2	⋯	⋯	<13.6	⋯	⋯

Table B1
(Continued)

QSO	ID	$N_{\rm gal}$	$z_{\rm gal}$	$\log M_{\rm star}$ $/M_\odot$	SFR $M_\odot\ {\rm yr}^{-1}$	$d_{\rm proj}$ kpc	$d_{\rm proj}$ $/r_{200}$	$\log\psi/G$ $/(M_\odot/{\rm kpc})$	$\log N_{\rm OVI}$ $/{\rm cm}^{-2}$	$\sigma_{\rm OVI}$ km s^{-1}	$v_{\rm OVI}$ km s^{-1}	$\log N_{\rm NeVIII}$ $/{\rm cm}^{-2}$	$\sigma_{\rm NeVIII}$ km s^{-1}	$v_{\rm NeVIII}$ km s^{-1}
J0110	s91	2	0.6803	9.6 ± 0.1	1.7 ± 0.4	147	1.49	9.4	$13.59^{+0.09}_{-0.11}$	$31.7^{+7.7}_{-7.0}$	$-40.8^{+8.8}_{-8.1}$	<13.1	⋯	⋯
J0154	s92	1	0.6824	9.4 ± 0.2	1.1 ± 0.3	189	1.99	9.0	<13.3	⋯	⋯	<13.4	⋯	⋯
J0248	s93	1	0.6885	8.7 ± 0.2	<0.1	195	2.52	8.8	<13.3	⋯	⋯	<13.1	⋯	⋯
J0111	s94	1	0.6898	10.9 ± 0.1	<0.2	372	1.66	9.9	<13.0	⋯	⋯	⋯	⋯	⋯
J0357	s95	5	0.6922	$8.7^{+0.3}_{-0.5}$	0.1 ± 0.1	98	1.27	10.9	<13.9	⋯	⋯	<13.6	⋯	⋯
J0454	s96	2	0.6938	10.6 ± 0.1	<0.2	392	2.71	9.4	<13.4	⋯	⋯	<13.3	⋯	⋯
J0333	s97	1	0.6945	10.5 ± 0.1	0.2 ± 0.2	307	2.21	9.3	$14.28^{+0.05}_{-0.05}$	$15.2^{+2.7}_{-2.3}$	$63.1^{+2.0}_{-2.1}$	<13.6	⋯	⋯
J0357	s98	4	0.7043	8.9 ± 0.2	0.4 ± 0.2	188	2.30	9.7	<13.0	⋯	⋯	<13.4	⋯	⋯
J0420	s99	2	0.7046	10.8 ± 0.1	<0.1	295	1.60	9.8	$14.06^{+0.19}_{-0.10}$	<24.6	$-66.5^{+5.3}_{-3.4}$	<13.6	⋯	⋯
J2135	s100	1	0.7046	$10.2^{+0.1}_{-0.2}$	0.3 ± 0.2	346	2.86	9.1	<13.6	⋯	⋯	⋯	⋯	⋯
J0248	s101	4	0.7062	9.7 ± 0.1	2.0 ± 0.4	227	2.25	10.3	$13.91^{+0.09}_{-0.10}$	<44.0	$140.6^{+7.9}_{-10.0}$	<13.6	⋯	⋯
J0110	s102	3	0.7092	11.3 ± 0.1	0.6 ± 0.3	1186	2.83	10.3	<13.2	⋯	⋯	<13.6	⋯	⋯
J0119	s103	6	0.7182	11.4 ± 0.1	<0.2	674	1.38	10.9	<13.2	⋯	⋯	<13.5	⋯	⋯

ORCID iDs

Zhijie Qu https://orcid.org/0000-0002-2941-646X
Hsiao-Wen Chen https://orcid.org/0000-0001-8813-4182
Sean D. Johnson https://orcid.org/0000-0001-9487-8583
Gwen C. Rudie https://orcid.org/0000-0002-8459-5413
Fakhri S. Zahedy https://orcid.org/0000-0001-7869-2551
Joop Schaye https://orcid.org/0000-0002-0668-5560
Erin T. Boettcher https://orcid.org/0000-0003-3244-0409
Sebastiano Cantalupo https://orcid.org/0000-0001-5804-1428
Jennifer I-Hsiu Li https://orcid.org/0000-0002-0311-2812
John S. Mulchaey https://orcid.org/0000-0003-2083-5569
Marc Rafelski https://orcid.org/0000-0002-9946-4731

References

Appleby, S., Davé, R., Sorini, D., Cui, W., & Christiansen, J. 2023, MNRAS, 519, 5514
Astropy Collaboration, Robitaille, T. P., Tollerud, E. J., et al. 2013, A&A, 558, A33
Bacon, R., Accardo, M., Adjali, L., et al. 2010, Proc. SPIE, 7735, 773508
Behroozi, P., Wechsler, R. H., Hearin, A. P., & Conroy, C. 2019, MNRAS, 488, 3143
Bergeron, J., Aracil, B., Petitjean, P., & Pichon, C. 2002, A&A, 396, L11
Blanton, M. R., & Roweis, S. 2007, AJ, 133, 734
Boettcher, E., Chen, H.-W., Zahedy, F. S., et al. 2021, ApJ, 913, 18
Burchett, J. N., Tripp, T. M., Prochaska, J. X., et al. 2019, ApJL, 877, L20
Carnall, A. C., McLure, R. J., Dunlop, J. S., & Davé, R. 2018, MNRAS, 480, 4379
Chen, H.-W., Lanzetta, K. M., Webb, J. K., & Barcons, X. 1998, ApJ, 498, 77
Chen, H.-W., & Mulchaey, J. S. 2009, ApJ, 701, 1219
Chen, H.-W., Wild, V., Tinker, J. L., et al. 2010, ApJL, 724, L176
Chen, H.-W., Zahedy, F. S., Boettcher, E., et al. 2020, MNRAS, 497, 498
Chen, H.-W., Zahedy, F. S., Johnson, S. D., et al. 2018, MNRAS, 479, 2547
Cooper, T. J., Rudie, G. C., Chen, H.-W., et al. 2021, MNRAS, 508, 4359
Danforth, C. W., Keeney, B. A., Tilton, E. M., et al. 2016, ApJ, 817, 111
Danforth, C. W., & Shull, J. M. 2008, ApJ, 679, 194
Donahue, M., & Voit, G. M. 2022, PhR, 973, 1
Dressler, A., Bigelow, B., Hare, T., et al. 2011, PASP, 123, 288
Dutta, R., Fumagalli, M., Fossati, M., et al. 2020, MNRAS, 499, 5022
Dutta, R., Fumagalli, M., Fossati, M., et al. 2021, MNRAS, 508, 4573
Faerman, Y., Sternberg, A., & McKee, C. F. 2020, ApJ, 893, 82
Faucher-Giguère, C.-A. 2020, MNRAS, 493, 1614
Faucher-Giguère, C.-A., & Oh, S. P. 2023, ARA&A, 61, 131
Foreman-Mackey, D., Hogg, D. W., Lang, D., & Goodman, J. 2013, PASP, 125, 306
Fossati, M., Fumagalli, M., Lofthouse, E. K., et al. 2019, MNRAS, 490, 1451
Fumagalli, M., Patel, S. G., Franx, M., et al. 2012, ApJL, 757, L22
Gehrels, N. 1986, ApJ, 303, 336
Gnat, O. 2017, ApJS, 228, 11
Green, J. C., Froning, C. S., Osterman, S., et al. 2012, ApJ, 744, 60
Gronke, M., Oh, S. P., Ji, S., & Norman, C. 2022, MNRAS, 511, 859
Haardt, F., & Madau, P. 2001, in Clusters of Galaxies and the High Redshift Universe Observed in X-rays, ed. D. M. Neumann & J. T. V. Tran, 64
Hafen, Z., Faucher-Giguère, C.-A., Anglés-Alcázar, D., et al. 2019, MNRAS, 488, 1248
Harris, C. R., Millman, K. J., van der Walt, S. J., et al. 2020, Natur, 585, 357
Ho, S. H., Martin, C. L., & Schaye, J. 2021, ApJ, 923, 137
Huang, Y.-H., Chen, H.-W., Johnson, S. D., & Weiner, B. J. 2016, MNRAS, 455, 1713
Huang, Y.-H., Chen, H.-W., Shectman, S. A., et al. 2021, MNRAS, 502, 4743
Hunter, J. D. 2007, CSE, 9, 90
Hussain, T., Khaire, V., Srianand, R., Muzahid, S., & Pathak, A. 2017, MNRAS, 466, 3133
Johnson, S. D., Chen, H.-W., Mulchaey, J. S., Schaye, J., & Straka, L. A. 2017, ApJL, 850, L10
Johnson, S. D., Chen, H.-W., & Mulchaey, J. S. 2015, MNRAS, 449, 3263
Kennicutt, R. C. J. 1998, ARA&A, 36, 189
Kewley, L. J., Geller, M. J., & Jansen, R. A. 2004, AJ, 127, 2002
Khaire, V., & Srianand, R. 2019, MNRAS, 484, 4174
Kravtsov, A. V., Vikhlinin, A. A., & Meshcheryakov, A. V. 2018, AstL, 44, 8
Kroupa, P. 2001, MNRAS, 322, 231
Lehner, N., Zech, W. F., Howk, J. C., & Savage, B. D. 2011, ApJ, 727, 46
Lofthouse, E. K., Fumagalli, M., Fossati, M., et al. 2020, MNRAS, 491, 2057
McQuinn, M., & Werk, J. K. 2018, ApJ, 852, 33
Meiring, J. D., Tripp, T. M., Werk, J. K., et al. 2013, ApJ, 767, 49
Mulchaey, J. S., & Chen, H.-W. 2009, ApJL, 698, L46
Muzahid, S., Schaye, J., Cantalupo, S., et al. 2021, MNRAS, 508, 5612
Muzahid, S., Srianand, R., Bergeron, J., & Petitjean, P. 2012, MNRAS, 421, 446
Narayanan, A., Savage, B. D., Wakker, B. P., et al. 2011, ApJ, 730, 15
Narayanan, A., Savage, B. D., & Wakker, B. P. 2012, ApJ, 752, 65
Navarro, J. F., Frenk, C. S., & White, S. D. M. 1996, ApJ, 462, 563
Nelson, D., Kauffmann, G., Pillepich, A., et al. 2018, MNRAS, 477, 450
Oppenheimer, B. D., Crain, R. A., Schaye, J., et al. 2016, MNRAS, 460, 2157
Oppenheimer, B. D., & Schaye, J. 2013, MNRAS, 434, 1043
Persson, S. E., Murphy, D. C., Smee, S., et al. 2013, PASP, 125, 654
Planck Collaboration, Aghanim, N., Akrami, Y., et al. 2020, A&A, 641, A6
Pointon, S. K., Nielsen, N. M., Kacprzak, G. G., et al. 2017, ApJ, 844, 23
Price-Whelan, A. M., Sipőcz, B. M., Günther, H. M., et al. 2018, AJ, 156, 123
Qu, Z., & Bregman, J. N. 2016, ApJ, 832, 189
Qu, Z., & Bregman, J. N. 2018, ApJ, 856, 5
Qu, Z., Chen, H.-W., Rudie, G. C., et al. 2022, MNRAS, 516, 4882
Qu, Z., Chen, H.-W., Rudie, G. C., et al. 2023, MNRAS, 524, 512
Rahmati, A., Schaye, J., Crain, R. A., et al. 2016, MNRAS, 459, 310
Rudie, G. C., Steidel, C. C., Pettini, M., et al. 2019, ApJ, 885, 61
Sameer, Charlton, J. C., Norris, J. M., et al. 2021, MNRAS, 501, 2112
Sankar, S., Narayanan, A., Savage, B. D., et al. 2020, MNRAS, 498, 4864
Savage, B. D., Kim, T.-S., Wakker, B. P., et al. 2014, ApJS, 212, 8
Savage, B. D., Lehner, N., Wakker, B. P., Sembach, K. R., & Tripp, T. M. 2005, ApJ, 626, 776
Schaller, M., Frenk, C. S., Bower, R. G., et al. 2015, MNRAS, 451, 1247
Schroetter, I., Bouché, N. F., Zabl, J., et al. 2021, MNRAS, 506, 1355
Sembach, K. R., Wakker, B. P., Savage, B. D., et al. 2003, ApJS, 146, 165
Simcoe, R. A., Sargent, W. L. W., & Rauch, M. 2004, ApJ, 606, 92
Stern, J., Faucher-Giguère, C.-A., Hennawi, J. F., et al. 2018, ApJ, 865, 91
Stern, J., Fielding, D., Faucher-Giguère, C.-A., & Quataert, E. 2019, MNRAS, 488, 2549
Stern, J., Fielding, D., Hafen, Z., et al. 2024, MNRAS, 530, 1711
Stocke, J. T., Keeney, B. A., Danforth, C. W., et al. 2014, ApJ, 791, 128
Stocke, J. T., Keeney, B. A., Danforth, C. W., et al. 2017, ApJ, 838, 37
Tchernyshyov, K., Werk, J. K., Wilde, M. C., et al. 2022, ApJ, 927, 147
Tchernyshyov, K., Werk, J. K., Wilde, M. C., et al. 2023, ApJ, 949, 41
Tepper-García, T., Richter, P., & Schaye, J. 2013, MNRAS, 436, 2063
Thom, C., & Chen, H.-W. 2008, ApJ, 683, 22
Tripp, T. M., Meiring, J. D., Prochaska, J. X., et al. 2011, Sci, 334, 952
Tripp, T. M., Sembach, K. R., Bowen, D. V., et al. 2008, ApJS, 177, 39
Virtanen, P., Gommers, R., Oliphant, T. E., et al. 2020, NatMe, 17, 261
Werk, J. K., Prochaska, J. X., Cantalupo, S., et al. 2016, ApJ, 833, 54
Werk, J. K., Prochaska, J. X., Thom, C., et al. 2013, ApJS, 204, 17
Werk, J. K., Prochaska, J. X., Tumlinson, J., et al. 2014, ApJ, 792, 8
Wijers, N. A., Faucher-Giguère, C.-A., Stern, J., Byrne, L., & Sultan, I. 2024, arXiv:2401.08776
Wijers, N. A., Schaye, J., & Oppenheimer, B. D. 2020, MNRAS, 498, 574
Wilde, M. C., Werk, J. K., Burchett, J. N., et al. 2021, ApJ, 912, 9
Yan, R., Newman, J. A., Faber, S. M., et al. 2006, ApJ, 648, 281
York, D. G. 1974, ApJL, 193, L127
Zahedy, F. S., Chen, H.-W., Cooper, T. M., et al. 2021, MNRAS, 506, 877
Zahedy, F. S., Chen, H.-W., Johnson, S. D., et al. 2019, MNRAS, 484, 2257
Zahedy, F. S., Chen, H.-W., Rauch, M., Wilson, M. L., & Zabludoff, A. 2016, MNRAS, 458, 2423
Zheng, Y., Faerman, Y., Oppenheimer, B. D., et al. 2024, ApJ, 960, 55